

3D radiative hydrodynamic simulations of protostellar collapse with H-C-O dynamical chemistry

Natalia Dzyurkevich¹, Benoît Commerçon², Pierre Lesaffre¹, Dimitry Semenov³

¹ Laboratoire de Radioastronomie Millimétrique, UMR 8112 du CNRS, École Normale Supérieure et Observatoire de Paris, 24 rue de Lhomond, 75231, Paris Cedex 05, France

² École Normale Supérieure de Lyon, CRAL, UMR 5574 du CNRS, Université de Lyon I, 46 allée d'Italie, 69364, Lyon Cedex 07, France

³ Max-Planck-Institut für Astronomie, Königstuhl 17, 69117 Heidelberg, Germany

ABSTRACT

Context. Combining the co-evolving chemistry, hydrodynamics and radiative transfer in protostellar collapse simulation is a major achievement, for both observations and theoretical developments in star formation studies. First, it allows a better link to observations, such as CO₂ and OH lines in the infrared. Second, a detailed knowledge of self-consistent chemical evolution for the main charge carriers (both gas species and dust grains) allows to correctly estimate the rate and nature of magnetic dissipation in the collapsing core.

Aims. We aim to describe the chemo-dynamical evolution of collapsing dense cores using a reduced gas-grain chemical network, which describes mainly H-C-O chemistry. We study the effect of free-fall time and of dust properties on the chemical evolution, i.e. the dynamical versus static chemistry.

Methods. We present the results of 3D simulations of 1 M_⊙ isolated dense core collapse. The physical setup includes radiative hydrodynamics and dynamical evolution of a chemical network. In order to perform those simulations, we merged the multi-dimensional adaptive-mesh-refinement code **RAMSES** and the thermo-chemistry Paris-Durham shock (PDS) code. We simulate the formation of the first hydro-static core and the co-evolution of 56 species, mainly describing H-C-O chemistry for the sake of computational feasibility.

Results. We have systematically tested the reduced chemical network against a well-established complex network. We show that by using a compact set of reactions, one can get a pretty good match with a much more complex network. This saves computational time and enables the chemo-dynamical RHD simulations of the cloud collapse in 3D. Our main results are threefold. (a) We follow in detail the time-dependent formation of the first hydro-static core, until the central temperature of about 800 K and density of about 10¹³ cm⁻³ were reached. After that, we use the output physical structure and apply the static gas-grain chemistry. with an extended set of reactions. We find that gas-grain chemistry post-processing can lead to one order of magnitude lower CO gas-phase abundances compared to the reduced dynamical chemistry, with strongest effect during the isothermal phase of collapse. (b) The duration of the isothermal phase (i.e. free-fall time) has little effect on the chemical abundances for our choice of the parameters. For mean grain sizes of 1 μm and larger, the gas-dust interaction timescales become longer than the representative dynamical timescales, which affects the pace of molecular depletion and makes dynamical chemistry a must. (c) Furthermore, dust mean size and size distribution have a strong effect on chemical abundances and hence on the ionization degree and magnetic dissipation. We present the ionisation profile for the collapsing cloud.

Conclusions. Dynamical chemical evolution is required to describe the CO gas phase abundance as well as the CO ice formation for the mean grain size larger than 1 μm. The latter point is of primary importance regarding the recent observational and theoretical evidences of the dust grain growth in the envelope of the protostellar cores. We conclude that proper accounting for dust grain growth in the collapse simulations can be as important as coupling the collapse with chemistry.

Key words. chemistry — hydrodynamics — radiative transfer

1. Introduction

There is hardly any other astrophysical topic linked to so many research fields in astronomy as star formation which involves a large variety of physical processes. Star formation is a key process to study the evolution of galaxies, the physics of the interstellar medium, the structure of molecular clouds, and the birth and evolution of planetary systems. Among others, chemistry is expected to play a crucial role during the star formation process: it regulates the thermal budget of the gas via atomic and molecular emission lines, as well as the degree of ionization of the gas, including

the grain charging. A precise description of the ionisation in star forming regions is required to follow accurately the coupling between the gas and magnetic fields, which has some important consequences regarding the long-standing problems of angular momentum and magnetic flux conservation in star formation.

Understanding the star formation process thus requires the coupling of chemistry with radiative magnetohydrodynamics (MHD) models which combine the effects of gravity, hydrodynamics, radiative transfer, and magnetic fields. The aim of such new generation of numerical models integrating chemistry is threefold: follow the main molecular tracers of

physical conditions (e.g. the lines of CO, C¹⁸O, HCO⁺), describe the coupling between gas and magnetic fields, and account for the thermal feedback of chemistry. In this study about protostellar collapse, we will focus on the first aspect, leaving the question of the coupling between gas and magnetic fields to subsequent paper.

Chemistry is first necessary to follow the evolution of the chemical tracers of physical conditions during the collapse, in order to compare models with observations and thus to verify or falsify the models. The chemistry of pre-stellar cores has been studied extensively (e.g. di Francesco et al. 2007; Bergin & Tafalla 2007). There have been several studies applying chemical modelling to either observed dense clouds or to more general models of isolated collapsing cores. Gas-grain chemical networks are usually massive and the resulting abundances are obtained at high computational costs (Hincelin et al. 2013). For this reason many researchers choose to use analytical or semi-analytical models for the dynamical evolution (e.g. Aikawa et al. 2008). With this simplification, Visser et al. (2009, 2011) could follow the chemo-dynamical evolution during protostellar collapse up to the formation of a disk around the protostar. Similarly, Maret et al. (2013) applied a large chemical network to a static spherical dense cloud at temperature 10 K and at density of about 10⁴ cm⁻³, adopting physical parameters close to the L1498 and L1517B prestellar cores. They explored the impact of dust size and of proper treatment of cosmic ray propagation on the chemistry, comparing their synthetic maps with available observations. The most advanced works, which combine the evolution of a full gas-grain chemical network together with 3D (radiation-)MHD models can be found in Furuya et al. (2012) and Hincelin et al. (2013). They calculated the chemical evolution of gas parcels linked to tracer particles, which described the different components of the collapsing core: envelope, pseudo-disk, disk, outflow, and the first hydrostatic core (FHSC Larson 1969).

All these chemo-dynamical models are in fact post-processing of hydrodynamic models/simulations. It allows the best link to observations, reproducing accurately the chemical abundances for given physical parameters. But, the feedback of the chemical abundances onto radiative and magneto-hydrodynamical evolution is neglected. Here, we are seeking a possibility to obtain both a reasonable quality of chosen chemical species and to have an opportunity to use the information about ionization and ion spatial distribution directly in the radiative and resistive MHD simulations.

Our ambition here is to implement a dynamical chemical evolution for the radiation-(M)HD models of protostellar collapse. We merge the RAMSES code (Teyssier 2002) and the thermo-chemical Paris-Durham shock PDS code (Flower & Pineau des Forêts 2003; Lesaffre et al. 2005, 2013; Flower & Pineau des Forêts 2015). The long-term goal is twofold. First, we aim to reproduce well enough the CO abundance with a simple network, because CO lines are important for the gas cooling during the collapse. Second, we aim to use the number densities of the charge carriers for dynamical calculations of the magnetic diffusivities in the collapse simulations in follow-up studies. Here we present the details on the R-MHD and chemical codes and the first parameter study.

The paper is organised as follows. In section 2, we present the reduced chemical network we use for protostel-

Element	ALCHEMIC	RAMSES
Gas-phase elements		
H ₂	0.5	0.5
He	0.09	0.09
C ⁺	1.2 × 10 ⁻⁴	1.2 × 10 ⁻⁴
O	2.56 × 10 ⁻⁴	2.56 × 10 ⁻⁴
N	7.6 × 10 ⁻⁵	-
S ⁺	8 × 10 ⁻⁸	-
Si ⁺	8 × 10 ⁻⁹	-
Na ⁺	2 × 10 ⁻⁹	-
Mg ⁺	7 × 10 ⁻⁹	-
Fe ⁺	3 × 10 ⁻⁹	3 × 10 ⁻⁹
P ⁺	2 × 10 ⁻¹⁰	-
Cl ⁺	1 × 10 ⁻⁹	-
Grain core elements		
O ^{**}	-	1.1 × 10 ⁻⁴
Si ^{**}	-	3.4 × 10 ⁻⁵
Mg ^{**}	-	3.7 × 10 ⁻⁵
Fe ^{**}	-	3.2 × 10 ⁻⁵
C ^{**}	-	7.3 × 10 ⁻⁴
<i>f</i> _{dg}	0.01	0.01085

Table 1. Elemental abundances used in ALCHEMIC (Semenov et al. 2010) and in RAMSES(PDS). Missing elements are shown with '-'. Elements C and O are partly depleted into grain cores. The grain core elements are used only in RAMSES, where the core abundances are given by $X[i_{\text{core}}] = X[i_{\text{solar}}] - X[i_{\text{gas}}]$. The choice of dust core abundances follows Godard et al. (2009); Lesaffre et al. (2013). The ALCHEMIC code does not allow assumptions about the dust composition (shown with '-').

lar collapse and the coupling of chemistry and radiation-hydrodynamics in RAMSES. Section 3 presents an application to protostellar collapse in which we study the effect of dust grain properties and dynamical time on the chemical state within the collapsing cloud. Section 4 concludes our work.

2. Methods and codes: chemistry in RAMSES

In this section we present the chemo-dynamical solver we have integrated in the adaptive-mesh-refinement (AMR) code RAMSES (Teyssier 2002). We first describe the reduced chemical network we design for protostellar applications and confront it against a full gas-grain chemical model. Then we present our implementation of dynamical chemistry in RAMSES.

2.1. The reduced chemical network

2.1.1. Chemical species

The chemical network we designed represents the main species and reactions necessary to describe CO abundances within mainly H-C-O chemistry in the early phases of protostellar collapse (Lesaffre et al. 2005). We include 14 neutral species (H, H₂, He, C, CH_x with $x = 1, \dots, 4$, O, O₂, H₂O, OH, CO, and CO₂), their corresponding single-charged positive ions, and ionized molecules CH₅⁺, H₃O⁺, HCO⁺, H₃⁺. In addition, iron is also included as a representative metal. We choose Fe because it has lower sublimation temperature than other metal-type species

(i.e. see Belloche et al. 2014, and complementary tables at www.astro.cornell.edu/~rgarrod/resources/). A similar reduced network was used in Wiebe et al. (2003) for the case of molecular clouds, showing that one can calculate the abundance of carbon monoxide and fractional ionisation accurately with significantly reduced chemical networks in the case of pure gas-phase chemistry.

We assume the solar total elemental abundance (Anders & Grevesse 1989; Godard et al. 2009), of which the major part of metals and a part of oxygen and carbon are depleted onto the grains (see Table 1 and Godard et al. 2009; Lesaffre et al. 2013). The dust grains contain O, Si, Mg, Fe and C as dust core elements. The size and mass of dust grains are calculated from the total mass of “dust-core” and “dust-mantle” elements and from the adopted size distribution. The number of dust grains are calculated as $n_{\text{dust}} = M_{\text{G,total}} / ((4/3)\pi\rho_{\text{solid}} \langle a \rangle^3)$, where ρ_{solid} is the internal density, $M_{\text{G,total}}$ is the total mass of the dust core elements, and $\langle a \rangle$ is the mean radius calculated using MRN size distribution $n(a) \propto a^{-3.5}$ (Mathis et al. 1977, see appendix A). Note that all dust core species do not participate in the chemical reactions and are used exclusively to calculate dust grain mass, because we neglect the core erosion processes in the frame of the presented models. All neutral species are allowed to freeze out on the dust grains, thus forming the grain mantles and increasing the weight of the grains. Last, we consider three type of grains, namely neutral (G), single-charged positive (G^+), and single-charged negative (G^-). Table 2 gives a summary of all the chemical species we include in our reduced chemical network. In total, the reduced chemical network describes the evolution of $N_{\text{species}} = 56$ species.

2.1.2. Chemical reactions

We include gas-phase, freeze-out, and sublimation reactions. We do not take into account other types of reactions such as soft X-ray ionisation which is important for low density (visual extinction $A_v \sim 0.2$, Wolfire et al. 1995). For protostellar collapse applications, A_v is already larger than 10 for a typical mass of $1 M_{\odot}$.

In total, our reduced gas-grain chemical network for H-C-O (and Fe as a representative metal) includes 231 reactions.

Gas-phase reactions. We include only reactions with two reactants. We use the classical Arrhenius representation for the reaction rate,

$$k_{\text{two}}(T) = \alpha \left(\frac{T}{300 \text{ K}} \right)^{\beta} \exp\left(-\frac{\gamma}{T}\right), \quad (1)$$

where α is the reaction rate at the room temperature, β characterizes the dependence on the gas temperature, and γ is the activation barrier. Most of the reactions constants we use have been downloaded from the online database KIDA¹ (Wakelam et al. 2012, see Sec. 2.2).

Recombination. Ions can be divided in two groups: the ones which recombine at relatively low rate (slow) with free electrons (Fe^+ , C^+ , He^+ , and H^+), and other ions (see Table 2)

which have up to three orders of magnitude higher recombination rate. To keep the network compact, we include the recombination reactions of all ‘slow’ ions and selected ‘fast’ ones: H_3^+ , CH_3^+ , CH_4^+ , CH_5^+ , O_2^+ , H_3O^+ , and HCO^+ . Similarly, the charge exchange between ions and neutral Fe takes place only with the most abundant ions: H^+ , C^+ , H_3^+ , O_2^+ , H_3O^+ , and HCO^+ . Charge transfer is also occurring via dust grains, for all ions, electrons and types of grains.

Photodissociation and ionization. The envelope of collapsing low-mass dense molecular cores is usually dense enough so that we can safely assume a visual extinction from the exterior of about $A_v \simeq 10$ as previously mentioned. The rate is calculated as

$$k = \alpha \exp(-\gamma A_v) G_0 S, \quad (2)$$

where G_0 is the far-UV (FUV) flux in units of the FUV interstellar radiation field of Draine (1978). The dissociation of H_2 and CO are calculated with mutual self-shielding, where S is a shielding factor which depends on the column densities of H_2 and CO. These shielding factors are necessary because the photodissociation of H_2 and CO occurs only through discrete absorption lines. The S -factor for H_2 depends on H_2 column density, whereas the shielding factor for CO depends on both H_2 and CO column densities, because some CO lines are shielded by H_2 lines. The column density is calculated as a sum of external and internal column densities. The external column density is a parameter to be chosen in initial conditions (see paragraph 3.1) and describes the properties of gas outside of the computational box, i.e. how deep the collapsing cloud is embedded into molecular clouds. The internal column density has to be calculated inside the collapsing cores, as described in Valdivia & Hennebelle (2014).

Gas-grain interaction. Dust properties (size, temperature, emissivity) are found to vary from one line of sight to another among diffuse and dense clouds (Steinacker et al. 2010). These observations indicate that dust grains evolve throughout the interstellar medium. They can grow by the formation of refractory or ice mantles, or by coagulation into aggregates in dense and turbulent regions. They can also be destroyed by fragmentation and erosion of their mantles under more violent conditions. Regarding the core-shine effect (Pagani et al. 2010), the Spitzer L183 images can be best reproduced, if the dust grows starting from an ‘initial’ mean radius $a_0 = 0.05 \mu\text{m}$ in the outer regions of dense clumps (for density $n \leq 3 \times 10^4 \text{ cm}^{-3}$, Steinacker et al. 2010). For higher densities, the mean dust radius increases proportionally to gas density. The dust growth models (Ossenkopf 1993; Ormel et al. 2009) show that dust can grow by forming fractal aggregates, which are then compacted, if the dark clumps are older than several of 10^6 years. Recent works (Andersen et al. 2013; Steinacker et al. 2014; Lefèvre et al. 2014) demonstrate that dust growth can also explain the observed core-shine in several objects, even if they are younger than 10^6 yrs. We do not consider dust growth here and adopt a fixed distribution of dust sizes. Keeping in mind the dust growth issue, we vary the dust size as a parameter to determine its importance for chemical abundances (see Table 3).

The neutral-dust reactions include freeze-out and desorption of species on(from) dust mantles. Dust can also in-

¹ kida.obs.u-bordeaux1.fr

Neutral species														
H	H ₂	He	C	CH	CH ₂	CH ₃	CH ₄	O	O ₂	OH	H ₂ O	CO	CO ₂	Fe
Ionized species														
H ⁺	H ₂ ⁺	H ₃ ⁺	He ⁺	C ⁺	CH ⁺	CH ₂ ⁺	CH ₃ ⁺	CH ₄ ⁺	CH ₅ ⁺	O ⁺	O ₂ ⁺	OH ⁺	H ₂ O ⁺	H ₃ O ⁺
CO ⁺	HCO ⁺	Fe ⁺												
Core species														
O ^{**}	Si ^{**}	Mg ^{**}	Fe ^{**}	C ^{**}										
Mantle species														
H [*]	H ₂ [*]	He [*]	C [*]	CH [*]	CH ₂ [*]	CH ₃ [*]	CH ₄ [*]	O [*]	O ₂ [*]	OH [*]	H ₂ O [*]	CO [*]	CO ₂ [*]	Fe [*]
Grains														
G	G ⁺	G ⁻												

Table 2. List of the chemical species included in the reduced chemical network.

teract with ions and electrons in charge-transfer reactions, which lead to neutralization of species. The freeze-out reaction rate is

$$k = \gamma \pi a^2 \sqrt{\frac{2k_B T}{m_{\text{dust}}}} s^{-1}, \quad (3)$$

where $m_{\text{dust}} = 4/3\pi a^3 \rho_{\text{solid}}$ with ρ_{solid} for internal density of dust grains. The thermal desorption rate is

$$k = q_\nu \exp\left(-\frac{\beta}{T}\right) s^{-1}, \quad (4)$$

where q_ν is the vibrational frequency and β is the critical temperature for thermal desorption of a specie. The charge exchange reaction rate is given by

$$k = \gamma \left(\frac{T}{300 \text{ K}}\right)^{0.5} \left(1 + \frac{450 \text{ K}}{T}\right) s^{-1}. \quad (5)$$

We exclude the reactions describing the formation of complex organic molecules on grain surfaces.

The elaborated treatment of dust, linking the mass and size to its core composition, allow us to evolve dust via erosion reactions. For collapse, it can become important when temperatures are rising above 800 K (chemo-erosion of C). In the hotter interior of the FHSC, the evaporation of Si^{**} and Fe^{**}, Mg^{**} can be accounted for. This will be used in future works. For the current study, we exclude dust-core erosion processes and keep the amount of solid material fixed (with the exception of ices, i.e. mantle species).

Cosmic ray (CR) ionization and desorption. We use a constant CR ionization rate ζ_{CR} in this paper. In reality, the impact ionisation by cosmic rays decreases with increasing density of the gas, because the cosmic rays, which follow magnetic field lines, have to cross a significant bulk of mass before reaching the dense regions in the inner part of the collapsing core (Padovani & Galli 2011). Cosmic rays may give rise to secondary electrons with energy of about 30 eV (Cravens & Dalgarno 1978), whereas the photons with energies of around 10 eV can ionize and dissociate species in the gas phase, as well as detach electrons from grains. These secondary electrons excite electronic states in H₂ via collisions, which result in ultraviolet fluorescence. The rates of photodissociation and photoionization are dependent on

the relative numbers of photons which are absorbed by the gas and by the dust. To describe the rates for ionization, dissociation or desorption induced by CR and secondary UV photons, we use

$$k_{\text{CR}} = \gamma \zeta_{\text{CR}} \left(\frac{T}{300 \text{ K}}\right)^\alpha, \quad (6)$$

where γ is the value of the reaction rate at the room temperature of 300 K, and α is zero for all species but CO. This unusual dependence of CR ionization on gas temperature is a 'short-cut', allowing to take into account CO dissociation by CR-induced secondary photons (see for details Gredel et al. 1987; Flower et al. 2007).

We include 21 reactions of ionization, which contain 9 reactions for the ionization of H, He, H₂ (with two ways), O₂, C, CO, CH₂ and CH₃, as well as 12 reactions for dissociation of H₂, CH, CH₃, CH₄ (two ways), CH⁺ (two ways), H₂O, O₂, OH, CO and CO₂.

Reaction rates for CR-desorption of the species from the dust surface is equivalent to thermal desorption (see eq. 4), under the assumption that CR heats the grain up to roughly 70 K (Semenov et al. 2010). We include 13 reactions since H₂ and He are released in the gas phase already at 10 K.

2.1.3. The chemistry module

We use the time-dependent chemistry PDS code, originally written for MHD shocks (Flower & Pineau des Forêts 2015, 2003; Lesaffre et al. 2004, 2005, 2013), which we have improved and successfully tested for physical conditions typical of the FHSC formation problem (see Sec. 2.2). Modelling of the chemical processes is described via a set of equations in the form

$$\partial_t n_x = -n_x \sum_r k_{rx} n_r + \sum_p \sum_q k_{pq} n_p n_q, \quad (7)$$

where n_x is the number density of a x chemical species. On the right hand, the negative term is the sum over the destruction reactions, and positive term is the sum over the reactions creating x -species from species p and q . k_{rx} and k_{pq} are the corresponding reaction rates. The cooling via molecular and atomic lines is present in PDS chemical code. In the context of this paper, we neglect the thermal

feedback of chemistry on the gas to concentrate on which parameters are affecting the coolant’s abundances.

We solve the system of equations (7) using either explicit or implicit integration in time. When the chemical time step is shorter than the hydrodynamical one, we use an implicit solver which consists in inverting the matrix of N_{species}^2 in size for a hydro(-magnetic) timestep of Δt_{hydro} . Should this not be the case, the chemical module switches to an explicit second-order Runge-Kutta method for time advancement.

In the implicit scheme, we use the DVODE solver², without any optimization of the matrix inversion procedure. There are indeed various optimization methods, like buffering, using the topology of matrix, flux method to remove slow reactions, or rates tabulation (Grassi et al. 2012, 2013). The highest possible speed gains here can be achieved for large networks, when using sparse representation of Jacobi matrix and sparse solvers of linear system of equations, like it is done in ALCHEMIC code (Semenov et al. 2010). According to our experience with the reduced network in RAMSES, those optimization methods can rather slow down the performance and even lead to the wrong abundances of the species, when applied blindly.

In this study, we present a set of models with non-optimized chemistry module, which shall serve as a benchmark for the upcoming optimized simulations. Typically, non-optimized chemo-dynamical simulation costs about 100 times more computational time compared to purely RHD collapse calculations.

The convergence control. The equations for chemical evolution are often stiff, i.e. having a large range of reaction time scales. In this case, the implicit solver will be used in the chemistry module. In this paragraph we briefly describe the solver and its convergence.

The chemistry solver proceeds in two steps: first, the hydrodynamical time-step Δt_{hydro} is divided into smaller chemical time-steps Δt_{chem} . Within the call of the DVODE solver, Δt_{chem} can also be reduced again automatically if the solver recognizes a problem (see ODEPACK package for details). The chemical solver stops when the sum of the intermediate Δt_{chem} reaches Δt_{hydro} . In each call of the DVODE solver, the set of equation (7) is integrated using Newton-Raphson iterations until convergence is obtained, which is controlled by the DVODE tolerance parameters ϵ_{tol} on the change of the absolute or relative abundancies ($\epsilon_{\text{tol}} = 10^{-6}$ typically).

2.2. Benchmarking of the reduced chemical network

In this section, we compare our reduced chemical network performance with the results of the full gas-grain chemical network ALCHEMIC (Semenov et al. 2010). We study the time evolution during 10^6 years of the chemical species for ‘0-D’ case, assuming constant gas density and temperature, $n = 10^4 \text{ cm}^{-3}$ and $T = 10 \text{ K}$. Our benchmark tests include pure gas-phase chemistry case, the case when all neutral species freeze out, and the case where both freeze-out and thermal desorption are included. We do not include the reactions responsible for the water formation on the dust surface, what saves the computational time. The limita-

tion here is an under-estimation of the total water abundance during the collapse simulation. The dust-surface reactions would lead to $X[\text{H}_2\text{O}] > X[\text{CO}]$ on the long term, i.e. when the molecular cloud is older than 1 Myr. The water molecules should be the main reservoir for oxygen in older clouds. In younger objects, CO is the dominant reservoir for oxygen.

At the beginning of benchmark tests, all initial chemical abundances including ices are set to 10^{-19} , except for H, H₂, O, Fe, C⁺, and the elements in the dust cores for which we follow (Godard et al. 2009, see Table 1 and 2). The dust-to-gas ratio f_{dg} is assumed 0.01 in ALCHEMIC, and calculated in RAMSES using $n_{\text{dust}}/n_{\text{H}} = 3 \times 10^{-12}$. We force the properties of dust to be exactly the same in both codes, fixing the dust size to be 0.1 μm .

There are some significant differences in the reaction coefficients which deserve to be justified. ALCHEMIC uses the reaction coefficients from the KIDA online data base. The reason for these differences in reaction coefficients in our network is that the network has been reduced ‘by hand’, compensating the missing reactions so that CO and HCO⁺ abundances could be obtained *very closely* to the abundances from full chemical network of ALCHEMIC. Thus, few coefficients in the reduced network are in fact *effective* coefficients.

In comparison to the original version of PDS code (Flower & Pineau des Forêts 2015; Lesaffre et al. 2005, 2013), we modify some reactions and partly update the reaction coefficients using the KIDA database. We have been then able to update the reaction involving H⁺ and CH₄ using KIDA coefficients to match closer match the ALCHEMIC’s relative abundances of these species. We also update the treatment of cosmic ray and thermal desorption following the work of Herbst & Osamura (2008).

To validate our reduced chemical network, we proceed in four steps with gradual increasing complexity in the chemistry. Intermediate results are presented in appendix B. First, we compare the results of the two different networks for the case of pure gas-chemistry and achieve a very good match except for CO₂ (fig. B.1). Then we add step-by-step adsorption on the grain surface (fig. B.2), and CR-desorption (fig. B.3). We observe very satisfactory agreement of the chemical evolution for all tests.

As the last step the thermal desorption is included in RAMSES code, and compared with full strength of ALCHEMIC code which includes also the formation of complex organics on the dust grains (fig. 1). The differences we observe in fig. 1 teach us when those reactions on the dust surface start to play a crucial role. Our conclusion is that our reduced network performs well for dust-free chemistry, and in the presence of dust on the timescale shorter than $10^6 - 10^7$ years. On the longer timescales, there are severe differences in the temporal evolution of the chemical abundances which are caused by missing species and reactions. For example, we have too much of iron in the ice form because we neglect FeH formation on the dust surface. The amount of water and CO₂ in ice form is lower compared to ALCHEMIC’s abundances, where the dust surface formation of water and other molecules is included. As our collapse is going to happen on much shorter time scale (free-fall timescale $\sim 10^4 - 10^5$ years), we suggest that the reduced network is fairly good for the simulations of dynamical chemistry during the dense cloud collapse.

² from the ODEPACK package downloadable at <https://computation.lnl.gov/casc/odepack/>

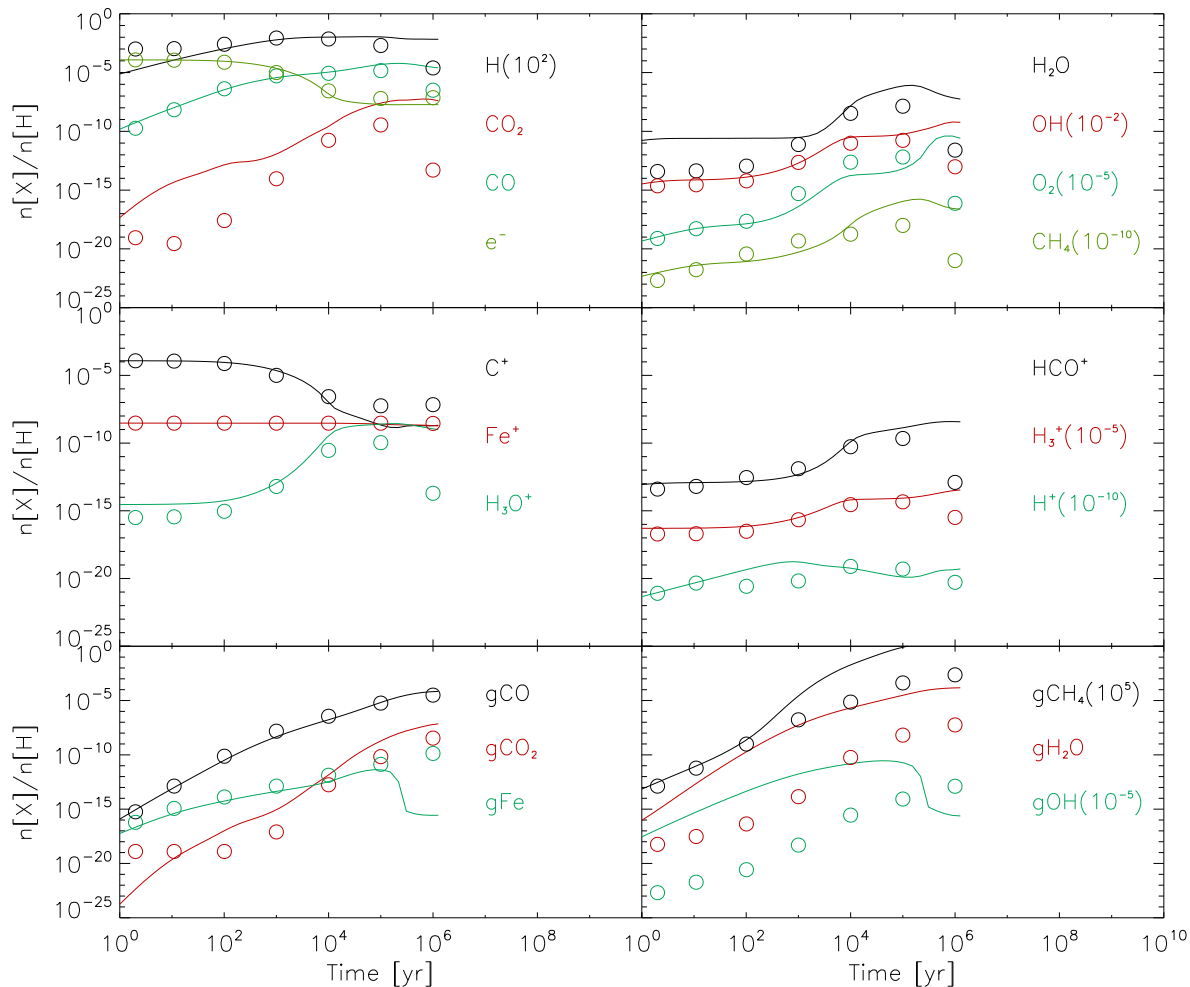


Fig. 1. Time evolution of selected species for complete set of gas-phase and gas-grain reactions (freeze-out on grain surface, CR and thermal desorption reactions). We plot a relative chemical abundances defined as $n[X]/n[H]$, where $n[H] = \rho_{\text{gas}}/m_p$ and m_p is the mass of proton. Solid line shows full chemical network ALCHEMIC (Semenov et al. 2010), circles show reduced network with RAMSES and PDS codes. Note that the full chemical network ALCHEMIC includes additional reactions between ices on the dust surface.

2.3. The chemo-radiation-magneto-hydrodynamic model

To perform 3D time-dependent chemical calculations of protostellar collapse, we coupled the time-dependent chemistry code PDS code (Flower & Pineau des Forêts 2015, 2003; Lesaffre et al. 2005, 2013) with the RAMSES code (Teyssier 2002).

2.3.1. The AMR RMHD code RAMSES

We use the radiation-magnetohydrodynamics (RMHD) solver of RAMSES. The MHD part of the code is based on the Constrained Transport (CT) scheme (Teyssier et al. 2006), using a 2D-Riemann solver to compute the electromotive force at cell edges (Fromang et al. 2006; Teyssier et al. 2006). In addition to the ideal MHD solver, ambipolar diffusion and Ohmic diffusion are also implemented as additional electromotive forces in the induction equation (Masson et al. 2012). For radiation transfer, we use the grey flux-limited diffusion (FLD) approximation described in detail in Commerçon et al. (2011b), which combines the explicit second-order Godunov solver of RAMSES for the hy-

drodynamical part, and an implicit scheme for radiative energy diffusion and coupling between matter and radiation terms. The implicit FLD solver uses adaptive time stepping (ATS, Commerçon et al. 2014) which enables us to benefit from the ATS scheme designed for the hydrodynamical part in RAMSES (Teyssier 2002). The gain in computational time over the former unique time step method ranges from 5 to 50 depending on level of adaptive time-stepping and on the problem.

2.3.2. The chemo-RHD solver

In this study, we neglect the effect of magnetic fields to concentrate on the dynamical evolution of chemistry coupled to an accurate description of the thermal balance of the gas during the collapse. The set of chemo-RHD equations solved in RAMSES with all radiative quantities estimated in

the co-moving frame are

$$\left\{ \begin{array}{l} \partial_t \rho + \nabla \cdot [\rho \mathbf{u}] = 0 \\ \partial_t \rho \mathbf{u} + \nabla \cdot [\rho \mathbf{u} \otimes \mathbf{u} + P \mathbb{I}] = -\lambda \nabla E_r \\ \partial_t E_T + \nabla \cdot [\mathbf{u} (E_T + P)] = -\mathbb{P}_r \nabla \cdot \mathbf{u} - \lambda \mathbf{u} \nabla E_r \\ \quad + \nabla \cdot \left(\frac{c\lambda}{\rho \kappa_R} \nabla E_r \right) \\ \partial_t E_r + \nabla \cdot [\mathbf{u} E_r] = -\mathbb{P}_r \nabla \cdot \mathbf{u} + \nabla \cdot \left(\frac{c\lambda}{\rho \kappa_R} \nabla E_r \right) \\ \quad + \kappa_P \rho c (a_R T^4 - E_r) \\ \partial_t n_x + \nabla \cdot [n_x \mathbf{u}] = -n_x \sum_r k_{rx} n_r \\ \quad + \sum_p \sum_q k_{pq} n_p n_q, \end{array} \right. \quad (8)$$

where ρ is the material density, \mathbf{u} the velocity, P the thermal pressure, κ_R the Rosseland mean opacity, λ the radiative flux limiter (e.g. Minerbo 1978), E_T the total energy $E_T = \rho \epsilon + 1/2 \rho u^2 + E_r$ (ϵ is the internal specific energy), κ_P the Planck opacity, E_r the radiative energy, and \mathbb{P}_r the radiation pressure. Note that compared to classical RHD solvers, we now have additional N_{species} equations on the number density of each specie n_x , which correspond to the advection, chemical creation and destruction of the x chemical elements.

Currently, the PDS chemical code has no impact on the evolution of the gas in RHD part of RAMSES. The possible limitations are then three-folds. First, the total gas and dust density ρ is not recomputed from the abundances obtained by the chemistry solver. This is not affecting our results, because we consider FHSC before the dust melting occurs above 800 K. Second, as mentioned previously, we do not include heating and cooling due to atomic and molecular lines, which should not be dominant as long as radiative transfer is dominated by the dust. Cooling by CO lines can be expected to become important for the gas densities of 10^3 cm^{-3} and lower. Last, we do not compute self-consistently the dust opacity from the dust composition given in output by the chemistry solver. For the latter, we instead use tabulated opacities from Semenov et al. (2003). All these limitations could be dealt by the combined RAMSES and PDS codes, but go far beyond the scope of the paper.

2.3.3. Requirement of element conservation.

The most strict and model-independent input for our chemistry code is the declaration of total elemental abundances, which we take equal to Solar abundances. They include oxygen, carbon, nitrogen, sulfur, and metals such as silicon, magnesium and iron. The maximal size of the chemical network include species involving those elements. Any time-dependent chemo-dynamical solver must guarantee total element abundances conservation *for each time step*, which can suffer from various numerical effects. First, element conservation is required during the chemical evolution. Second, the conservation has to be enforced during the advection.

The ‘‘consistency’’ subroutine is constructed so that after each advection operation the local elemental abundances are conserved (Modified Consistent Multi-fluid Advection). As pointed out in works by Glover et al. (2010), this is essential for correct evolution of chemistry.

The ‘‘consistency’’ check also takes into account the composition of dust, or the composition changes. In the case of sputtering of the species from the dust mantles or erosion of the dust core, the total amount of chemical elements in both gaseous and solid form is conserved.

3. Results for dense core collapse calculations

3.1. Initial conditions

Parameters of the core We choose a spherically-symmetric collapse configuration, i.e. we neglect rotation, magnetic fields and turbulence. The initial core mass is fixed to $1 M_\odot$ and the temperature of both gas and dust is uniform and equals 10 K. Note that in our model, we assume that the dust and gas are perfectly coupled thermally. The adiabatic index is $\gamma = 5/3$ and the mean molecular weight is $\mu_{\text{gas}} = 2.375$. In this paper we use both $n_{\text{gas}} = \rho_{\text{gas}} / (\mu_{\text{gas}} m_p)$ and $n[\text{H}] = n_{\text{gas}} \cdot \mu_{\text{gas}}$, where m_p is the mass of proton. It is common to represent the relative abundance of x chemical specie as $n[x]/n[\text{H}]$. In all our models, the initial density profile is Bonnor-Ebert like $n = n_c / (1 + (r/r_c))^{-2}$, where the maximum density in the center n_c is 10 times larger than the density at the core’s border. The total length of the simulation box is four times larger than the core initial radius r_0 .

Table 3 gives a summary of all the calculations we present in this study. In our fiducial model, labeled S1, the central density is $n_c = 4.4 \times 10^5 \text{ cm}^{-3}$ (or, $1.71 \times 10^{-18} \text{ g cm}^{-3}$), and the core radius is $r_0 = 0.022 \text{ pc}$. The relation between thermal and gravitational energies is $E_{\text{th}}/E_{\text{grav}} = 0.447$.

First, we add two more models, which have the initial core mass but different box length, i.e a factor two (S1x2) and four (S1x4) larger. The initial density and thus the free-fall time t_{ff} thus increases as the central density decreases. This affects the time available for the chemical reactions to evolve, especially affecting the abundances of ices (see Table 3). Second, we take the same core initial properties as model S1, but we vary the dust properties (models S2 to S5).

Choosing/generating initial chemical abundances Defining a good initial chemical abundance for a dense core is a topic in itself. The physics of dense core formation is not yet well understood. What is the lifetime of molecular cloud prior to collapse, how fast do dense core collapse, what happens to dust size distribution, what is the cosmic ray ionisation rate, the exposition to X-rays and UV photons? There are no precise answers to those questions. To simplify and focus on the effect of dynamical chemistry alone, we choose a uniform high visual extinction $A_v = 30$ and a uniform, cosmic ray ionization rate of $1.3 \times 10^{-17} \text{ s}^{-1}$. In order to generate the initial chemical abundances, we start from elemental abundances listed in Table 1 and let the chemistry evolve for 6×10^5 years in the static Bonner-Ebert sphere configuration (e.g. Hincelin et al. 2013). As mentioned previously, the assumptions about dust size distribution differs depending on the model (see Table 3). In the previous benchmarking results, we have tested the reduced network for $n_{\text{gas}} = 10^4 \text{ cm}^{-3}$ and $T = 10 \text{ K}$. We adopt similar value for the gas density in the fiducial model, with the central gas density order of magnitude higher. It can be easily shown, that the relative abundances of CO and gCO are very insensitive to the gas density if temperature remains of about 10K. The ratio of $n[\text{CO} + \text{gCO}]/n[\text{H}]$ remains about 10^{-4} for the whole range of the gas densities from 10^4 cm^{-3} to 10^{12} cm^{-3} , and is only limited by the availability of oxygen to form CO (see appendix D).

Model	$E_{\text{th}}/E_{\text{grav}}$	r_0 [pc]	$\sqrt{\langle a^2 \rangle}$ [μm]	$n_{\text{dust}}/n[\text{H}]$	$n_{\text{dust}} \langle a^2 \rangle / n[\text{H}]$	t_0 [kyr]	section
S1	0.45	0.022	0.1	3.1×10^{-12}	3.1×10^{-14}	57.8	Sec. 3.2
S1x2	0.89	0.045	0.1	3.1×10^{-12}	1.0×10^{-14}	455.0	Sec. 3.3
S1x4	1.79	0.088	0.1	3.1×10^{-12}	1.0×10^{-14}	1702.0	Sec. 3.3
S2 _{MRN}	0.45	0.022	0.05	3.9×10^{-12}	1.0×10^{-14}	57.8	Sec. 3.4
S3 _{MRN}	0.45	0.022	0.017	5.2×10^{-11}	1.5×10^{-14}	57.8	Sec. 3.4
S4	0.45	0.022	1.00	3.1×10^{-15}	3.1×10^{-15}	57.8	Sec. 3.4

Table 3. List of 3D chemo-dynamical calculations of collapse. The cloud is assumed to be always of one solar mass. S1 is a fiducial model. Model S1x2 and S1x4 are done for the collapse of the cloud of same mass but spreaded over larger calculation box L_{box} , i.e. core radius $r_0 = L_{\text{box}}/4$ is increasing factor 2 and 4, and so the relation between thermal and gravitation energy is altered. S2_{MRN}, S3_{MRN} are the models with MRN dust size distribution, whereas models S1, S4 have fixed grain size. $n_{\text{dust}} a^2$ represents mean dust cross-section.

Synchronization The properties of the FHSC are independent of the cloud mass and weakly affected by the temperature of the parental cloud (Vaytet et al. 2012). When we simulate the collapse of dense cores identical in all aspects except the initial density, the resulting FHSCs shall appear similar. Of course, each simulation will need different time to reach the FHSC depending on how dense it was initially, what may affect the chemical abundances. Thus, we define here as a zero-time t_0 the moment of the FHSC formation, i.e. when central density reaches 10^{13} cm^{-3} ($T \sim 210 \text{ K}$). The zero-time for different simulations is summarized in Table 3.

3.2. Fiducial model: evolution of chemical abundances during the collapse

Figure 2 shows the radial profiles for the fiducial run S1 of total density, temperature, and selected relative chemical abundances for five different times, from the start at -57.8 kyr and up to the moment when the central temperature exceeds 800 K at 0.99 kyr . At the beginning of the simulation, most of the neutral species are in the form of ice. After the FHSC formation, i.e. the beginning of the adiabatic phase, thermal desorption puts the neutrals back to gas phase. This ice sublimation starts inside at the edge of the future FHSC (8 to 10 AU) and proceeds outwards with time as the FHSC accretes mass and radiate away all the accretion luminosity (Commerçon et al. 2011a). The chemically-related ion abundances develop a flat-shaped local maximum at roughly the same location where related neutrals are evaporated from the dust surface. The pairs of $(\text{CO} - \text{HCO}^+)$, $(\text{H}_2\text{O} - \text{H}_3\text{O}^+)$, and $(\text{CH}_4 - \text{C}^+)$ show a correlation between evaporation of the molecule and a bump in the ion abundances.

In the bottom-right panel, we show the relative electron abundance profiles accompanied by relative abundances of negatively charged grains. For radii $r > 10 \text{ AU}$, the number of charged dust is small compared to main charge carries, so that $n_i \approx n_e$. The grey lines show the profiles $\propto n_{\text{gas}}^{1/2}$ and $\propto n_{\text{gas}}^{-1}$ for comparison. Profile $n_e \propto n_{\text{gas}}^{-1/2}$ originates from the early works on equilibrium ionization calculations (Elmegreen 1979; Fiedler & Mouschovias 1993). This fit is only valid when the gas density is smaller than 10^{10} cm^{-3} , i.e. where the role of dust as charge carrier is relatively weak. In fig. 2 we observe that indeed the electron abundance scales as $n_{\text{gas}}^{-1/2}$ for $r > 10 \text{ AU}$. In Machida et al. (2007), the electron abundance scales as n_{gas}^{-1} and represents

the scaling where charged dust is important. Machida et al. (2007) have considered much smaller dust size (distribution of dust grains with $a_{\text{min}} = 0.005 \mu\text{m}$ and $a_{\text{max}} = 0.25 \mu\text{m}$), what results in ion-dust dominated regime. Closer to the FHSC border, our electron abundances resemble n_{gas}^{-1} because of the increased role of negatively charged dust. The implications of ion-electron and ion-dust regimes for the magnetic diffusivities will be discussed in the subsequent paper.

We are now interested in the seemingly flat profile observed for the ratio $(n[\text{CO}] + n[\text{gCO}])/n_{\text{gas}}$ with radius. The isothermal phase of collapse takes most of the time, starting from $t_0 - 57.8 \text{ kyr}$ (start of the simulation) to roughly $t_0 - 1 \text{ kyrs}$. During this time, the abundances of CO and other molecules increase due to gas-phase reactions. We make an experiment to test whether the CO abundances can be reproduced with static chemical model, at least during the isothermal stage of collapse. We change the initial condition so that the chemical abundances in the initial cloud are 56.8 kyrs older than in S1 model, matching the age of the output with $t - 1 \text{ kyr}$. Then, we run a simulation with only adsorption and desorption on (from) the dust grain surface (model S1(D/A)). The species are thus just advected and can only freeze or melt on/from the dust surface (chemisorption of CO, see also Lesaffre et al. 2005). Figure 3 shows only a small difference between models with chemically evolved total CO abundances (S1) and the pre-evolved total CO in case of S1(D/A), if the temperature remains close to 10 K (3 bottom right, fig. 8 as well). The difference remains small in spite of significant increase in the gas densities close to the FHSC border, which is in agreement with the results of the evolution map of CO shown in Appendix D. This is also in agreement with the finding of Lesaffre et al. (2005) and adds a further justification for using the post-processing techniques to account for the *total* CO abundances.

When plotting the ratio of gaseous CO to its total abundance (fig. 3, bottom right), we can observe that stationary chemistry in S1(D/A) case underestimate the CO in the gas phase by more than one order of magnitude at radii $10^2 < r < 4 \times 10^3 \text{ AU}$. Gaseous CO is a tiny fraction of the total carbon monoxide abundance and this difference is invisible in fig. 3 bottom left. Thus, we note that post-processing with static chemistry may not be accurate enough to reproduce the abundance of CO in the gas phase.

After the temperature begin to rise within the FHSC, the total CO abundance increases by a factor of a few due to the faster reactions in the hotter gas. Above 60 K , the group of CH_x molecules is thermally desorbed from the grain sur-

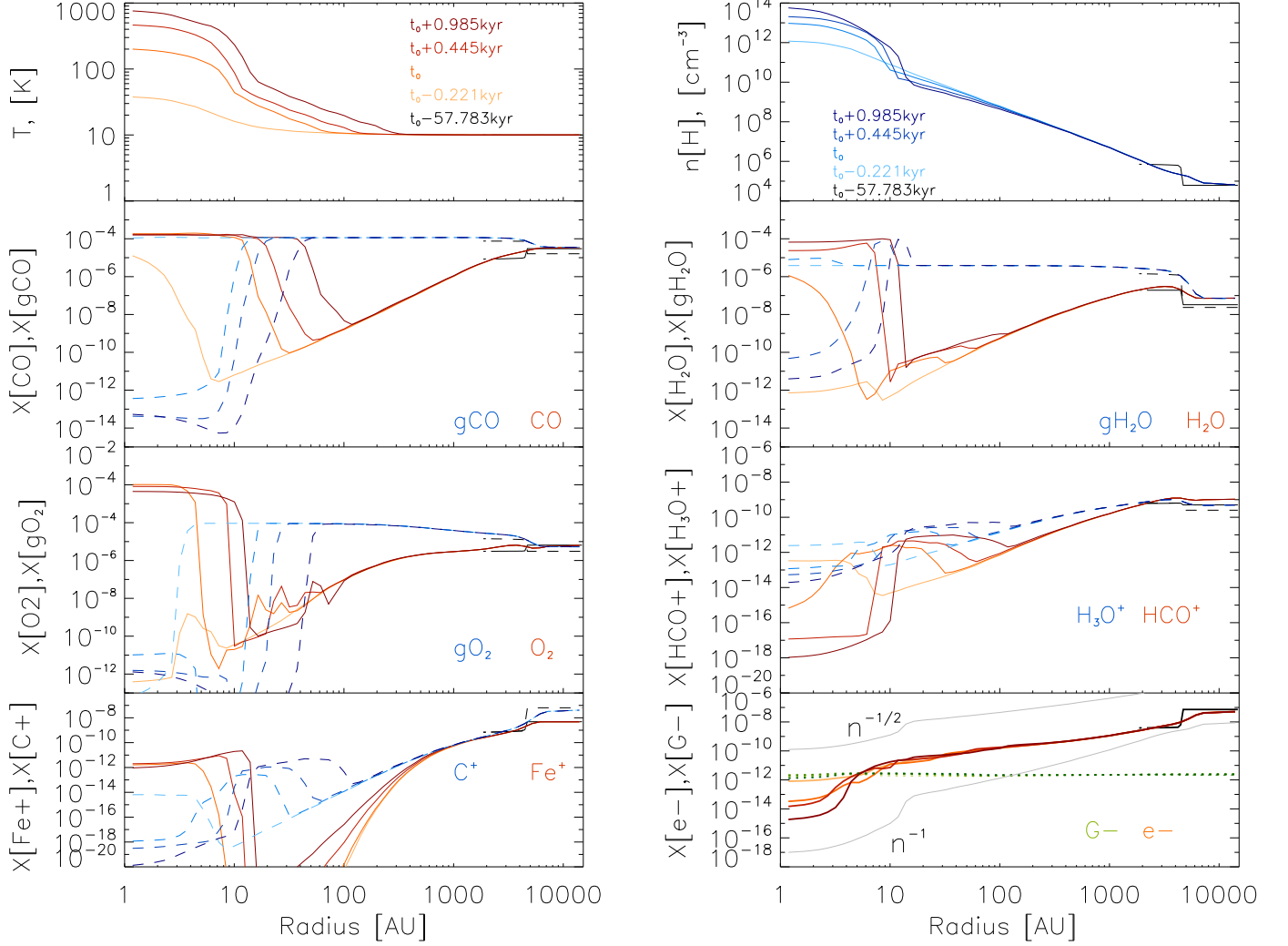
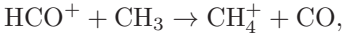
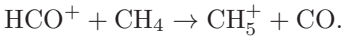


Fig. 2. Model S1: fiducial collapse model and corresponding time evolution of chosen species.

face. Hence, the abundance of CO increases by a factor of a few through the reactions



and



The steady-state chemisorption of CO will not apply inside of the core, or in regions where $T > 60$ K which can extend further in the disk and in the outflow found in rotating collapsing cores (e.g. Commerçon et al. 2010).

3.3. Impact of free-fall time on the chemical abundances in the FHSC

In this section, we investigate the effect of free-fall time on chemistry, i.e. the time for the chemistry to evolve prior to FHSC formation. Simulations runs S1x2 and S1x4 start with the same initial mass as fiducial model S1, but with a core radius two and four times larger so that the core's free-fall time increases as the initial density decreases (Table 3).

Figure 4 presents a direct comparison of selected chemical abundances at t_0 as in fig. 2. There is strikingly more ice available at t_0 in model with largest initial core radius, S1x4. Water ice is even reaching $n[\text{gH}_2\text{O}]/n[\text{gCO}] > 1$ in the low-density region. Note that, as mentioned in Sec. 2.2, we deliberately underestimate the amount of water ice due to the lack of the dust-surface reactions in our reduced chemical network.

We can observe the features which are common with the fiducial model. Again, the pairs of (CO – HCO⁺), (H₂O – H₃O⁺) and (CH₄ – C⁺) show correlation between evaporation of the molecule and the bump in the ion abundances. The abundance of CO is increasing only by a factor of a few with the age of the cloud. The total amount of CO seems to be a fixed fraction of gas density everywhere, which is partly an effect of the log-scale of the plots.

According to Lesaffre et al. (2005) and Eqs. (15)-(16) therein, the simple estimation of free-fall time and time of CO adsorption on dust grains (t_{AD}) allows to conclude that 'static chemisorption' of CO should be sufficient for the collapse simulations. In fig. 5, we plot the free-fall time and the CO adsorption time for models S1, S1x2, and S1x4 (see Table 3). As expected, the freeze-out of CO is happening

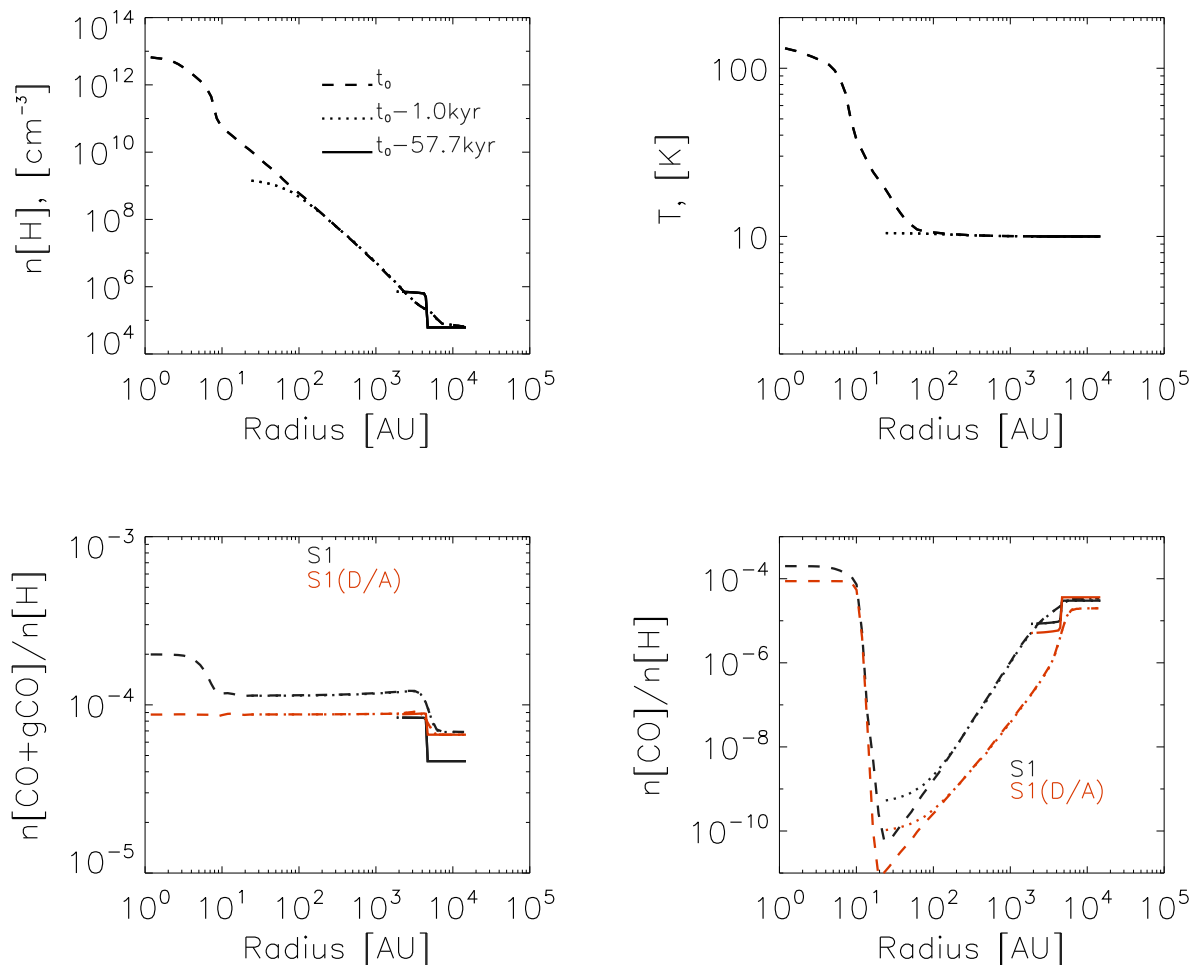


Fig. 3. Effect of dynamical chemistry on CO abundances. Top row: gas density and temperature radial profiles at three different times, shown with solid, dotted and dashed lines. Left bottom: Total (gas phase and ice) CO abundance profiles for the fiducial model S1 in black, and for the same collapse with advection of species but with only reactions of adsorption and desorption (model S1(D/A)), shown in red. Right bottom: fraction of gaseous CO for S1 and S1(D/A) models, same line and color coding.

faster than free-fall time almost everywhere in the cloud – for our choice of parameters. Figure 5, middle, shows the time of CO adsorption on dust grains (t_{AD}) for various dust sizes. If the dust has grown to larger sizes (as hinted by observed coreshine) then a dynamical treatment of CO may become necessary in the envelope (fig. 5, $t_{ff} < t_{AD}$).

The main effect of longer free-fall time is found in the behaviour of O_2 : whereas the ices are melted at the same location in all three models, the gas-phase O_2 appears at larger radii ($r > 20$ AU, outside of FHSC) in the models with the extended radii, S1x2 and S1x4, than in the fiducial run. In fiducial S1, the gas-phase abundance of O_2 shows a sharp decrease dip around 5-6 AU at t_0 . By comparing with other species, we find that a similar behaviour is exhibited by O_2^+ . At the same location, the abundance of C makes an anti-correlated bump in fiducial model S1. As the only difference is the tempo of the collapse, we conclude that this difference occurs due to dynamical effects. In fig. 5 we test this conclusion. The gas-phase reactions are usually slower than the reactions of adsorption-desorption on dust, as shown in fig. 5 (right) for the example of O_2 . We can see

that creation of O_2 is faster than free-fall time only in the fiducial model S1, and is slower in the extended-box models S1x2 and S1x4. This explains also why there is less gO_2 in the fiducial model.

Intriguingly, there was for a long time a discrepancy between chemical models of the ISM and O_2 non-detections by SWAS and ODIN space telescopes. The typical value of $X(O_2)$ in the models was $\sim 10^{-6}$, same as in our fiducial run. The solution to mismatch was to account for ice chemistry and water formation on grains. When it is included, it consumes elemental oxygen quite early after the start of chemical evolution in a diffuse ISM, making elemental O unavailable in large amounts to form significantly abundant molecular oxygen ($O_2/H_2 > 10^{-8}$). It is interesting, that a relatively fast collapsing cloud show similar effect - a lack of molecular oxygen within a certain radius, pointing out to a second possibility explaining the local absence of O_2 .

Last, the ionization fraction in fig. 4 are almost identical for simulations with different initial core radii, because the ionization equilibrium is reached in all simulations. In the center of the cloud, the dominant role of dust grains leads

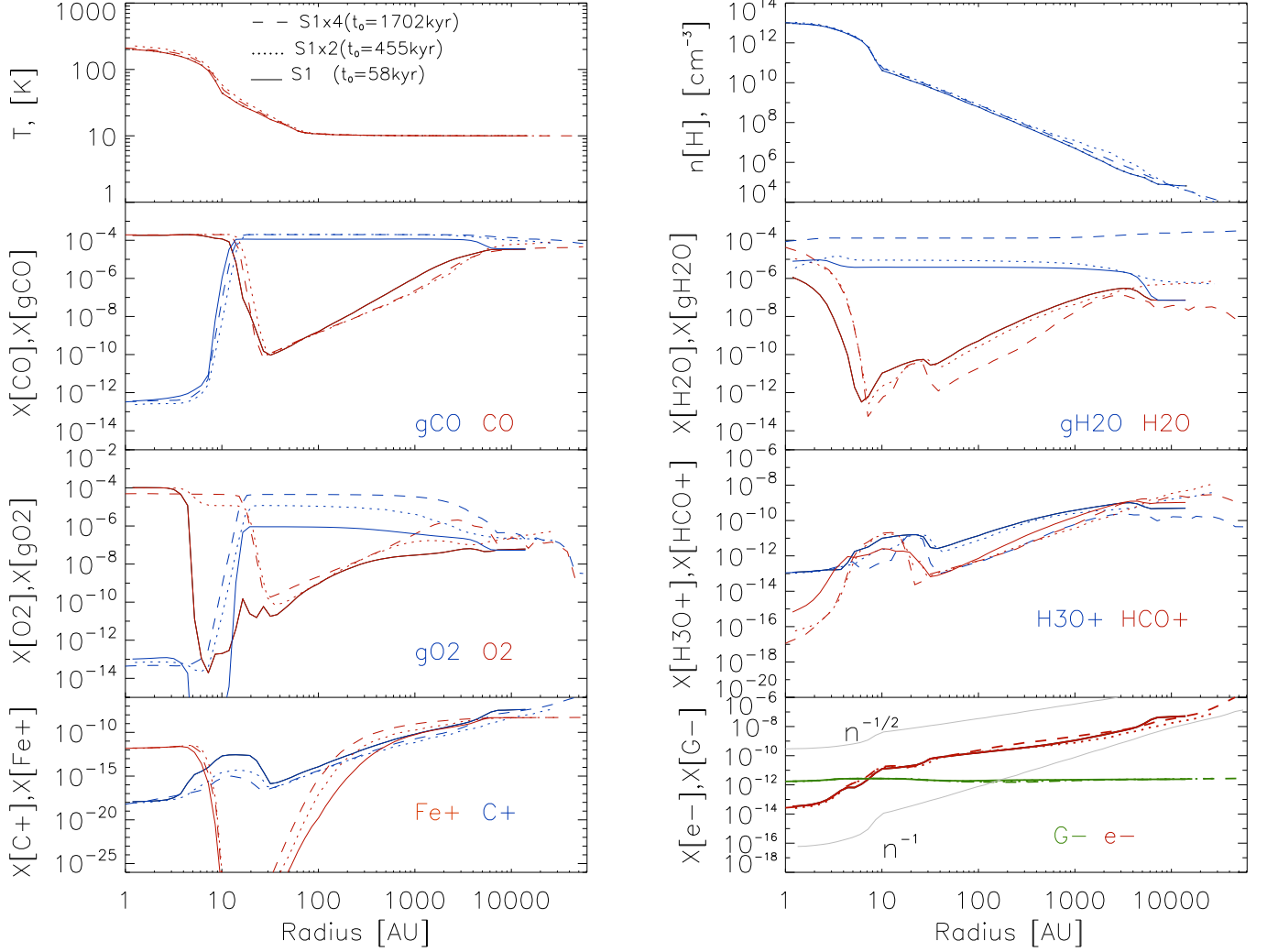


Fig. 4. Effect of free-fall time. Solid line shows fiducial model (S1), dotted line the model with twice as large box (S1x2), and the dashed line the model S1x4 with a box four times larger. In the top left window we provide the time t elapsed from the begin of simulation to the moment we choose as t_0 .

to fast equilibrium too, in spite of the rapidly changing hydrodynamical conditions.

3.4. Impact of dust and its properties on the chemical abundances in the FHSC

In this section, we compare four models with different dust size properties: models S1, S2_{MRN}, S3_{MRN}, and S4 (Table 3). S2_{MRN} and S3_{MRN} models make use of the MRN distribution for the grain sizes in the chemistry module. Model S4 has a fixed grain size (as in fiducial model S1) and serve as a boundary case, where we assume very large dust. Note that all the four models use identical set of chemical reactions, initial conditions and dust-to-gas ratio $f_{\text{dg}} = 0.01$, only the dust size properties are varied.

We refer the reader to Appendix A for a more complete description of the treatment of the dust size in RAMSES-PDS code. In the following, we briefly summarize the differences between these four models:

- S1** : Fiducial case has single-sized dust with $a_0 = 0.1\mu\text{m}$, dust-to-gas ratio, and dust density $n_{\text{dust}} = 3.09 \times 10^{-12}n_{\text{H}_2}$;
- S2_{MRN}** : We use the classical MRN dust grain size distribution $n_{\text{dust}}(a) \sim a^{-3.5}$ (Mathis et al. 1977), scaled to match the results of coreshine modelling (Steinacker et al. 2010). The mean dust radius is $\sqrt{\langle a^2 \rangle} = 0.05 \mu\text{m}$, what corresponds to $a_{\text{min}} = 2.6 \times 10^{-6} \text{cm}$ and $a_{\text{max}} = 5 \times 10^{-5} \text{cm}$. Fixing $f_{\text{dg}} = 0.01$, the dust number density is calculated to be $n_{\text{dust}} = 3.9 \times 10^{-12}n_{\text{H}_2}$ (see Appendix A for details);
- S3_{MRN}** : Same as S2_{MRN}, but we adopt $a_{\text{min}} = 10^{-6} \text{cm}$ and $a_{\text{max}} = 3 \times 10^{-5} \text{cm}$ (Flower & Pineau des Forêts 2003). The mean dust radius is $\sqrt{\langle a^2 \rangle} = 0.017\mu\text{m}$, and $n_{\text{dust}} = 5.24 \times 10^{-11}n_{\text{H}_2}$. This size range resembles the fit for mixed composition ‘large’ grains, made of bulk carbonaceous material, close to the range considered in (Mathis et al. 1977, PAH grains are not considered);
- S4** : Same as S1, i.e. single-sized dust, with $a_0 = 1\mu\text{m}$, and $n_{\text{dust}} = 3.09 \times 10^{-15}n_{\text{H}_2}$.

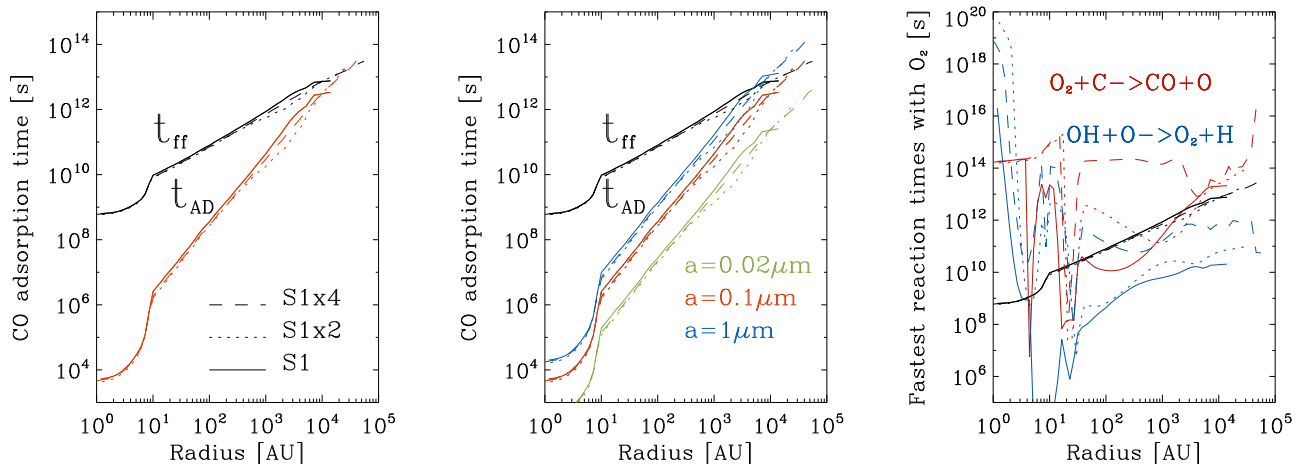


Fig. 5. Comparison between the free-fall time and adsorption time (on example of CO) at the moment of FHSC formation for different free. Left: Solid line shows fiducial model (S1), dotted line the model with twice as large box (S1x2), and the dashed line the model S1x4 with a box four times larger. Middle: For same models, we show with colors how the CO adsorption time varies with the dust size, where the dust number density is adopted according to Table 3. Right: Fastest reactions of creation and destruction of O_2 , for the same models.

Figure 6 shows the radial profiles of selected chemical species for models S1, S2_{MRN}, and S3_{MRN} at time t_0 . The dust properties, such as size distribution and total number density, have a significant impact on the resulting abundances of all species, especially ions and other charged species. We observe that the location and steepness of ice sublimation depends on the dust properties too, as visible on the plots showing H_2O and CO relative abundances: water can already be in the gas phase for fiducial model within the FHSC, but still not melted in S3_{MRN}. The thermal desorption needs indeed more energy to win against faster freeze-out processes in the case of larger dust number density experienced by the S3_{MRN} model.

In order to understand how dust properties affect the results, we shall concentrate on the reactions of charge transfer (eqs. 7, 5) and adsorption (eqs. 7, 3). The creation rate in case of charge transfer or recombination is proportional to n_{dust} . The creation rate for ice species is proportional to $\langle a^2 \rangle n_{\text{dust}}$. Whereas the dust density decreases steadily from model S1 to S3_{MRN}, the parameter $\langle a^2 \rangle n_{\text{dust}}$ is maximal for S1, followed by S3_{MRN}, with a minimum value in S2_{MRN} (see fig. 7). Naively, one could expect that amount of ice species should be maximal in fiducial model S1, as it has largest dust surface available, and an ionization degree should be maximal in fiducial model S1, followed by S2_{MRN} and S3_{MRN}. We observe that the fiducial model S1 has largest fraction of CO in solid form, but in case of water ice and gO_2 the 'ice' abundances are maximal for the model S3_{MRN}. Similarly confusing it is with the amount of electrons: We observe that electron fraction can be larger within the FHSC for the case of S2_{MRN}, accompanied by larger fraction of HCO^+ and H_3O^+ compared to fiducial model S1. Thus the ionization degree, abundances of ions and formation of ices strongly depend on the properties of dust, but to correlate the chemical abundances with the number and with the size distribution of dust is difficult.

Figure 8 shows when and how the abundance of CO is affected by the dust size and the dust number density. We plot the density and temperature radial profiles for the

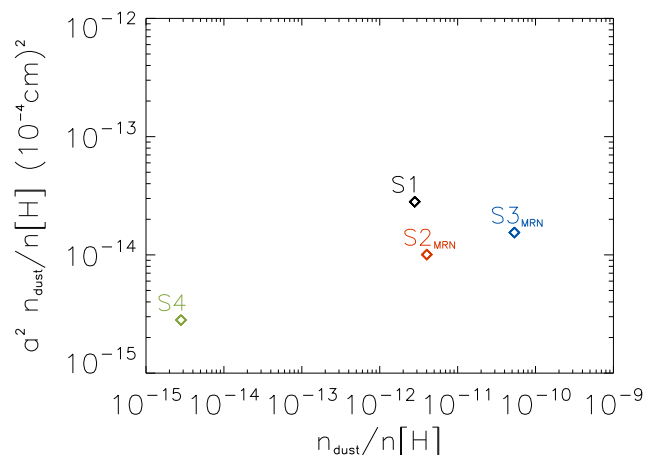


Fig. 7. Mean grain cross-section per hydrogen nucleus as a function of dust density n_{dust} for models S1, S4, S5, S2_{MRN} and S3_{MRN}. Model S2_{MRN} is taken closest to coreshine modelling.

initial conditions, at time t_0 (FHSC formation), and at one intermediate time characterizing the isothermal phase of the collapse. We show the corresponding radial distribution of gaseous and total CO abundance, $X[\text{CO}] = (n[\text{CO}] + n[g\text{CO}])/n_{\text{H}}$ for different dust grain size properties. The initial abundances are shown with thick lines. Already at this stage, the radial profile of $X[\text{CO}]$ differs dramatically with the dust size. In model S2_{MRN}, $X[\text{CO}]$ depends very weakly on the core radius (or gas density), but in models S1 and S4 it increases with gas density, and for S3_{MRN} it even decreases with gas density (observe solid lines in fig. 8 bottom left).

The isothermal phase of the collapse is taking about 5×10^4 years in the fiducial case. There is only about thousand years 'left' to reach the FHSC formation during

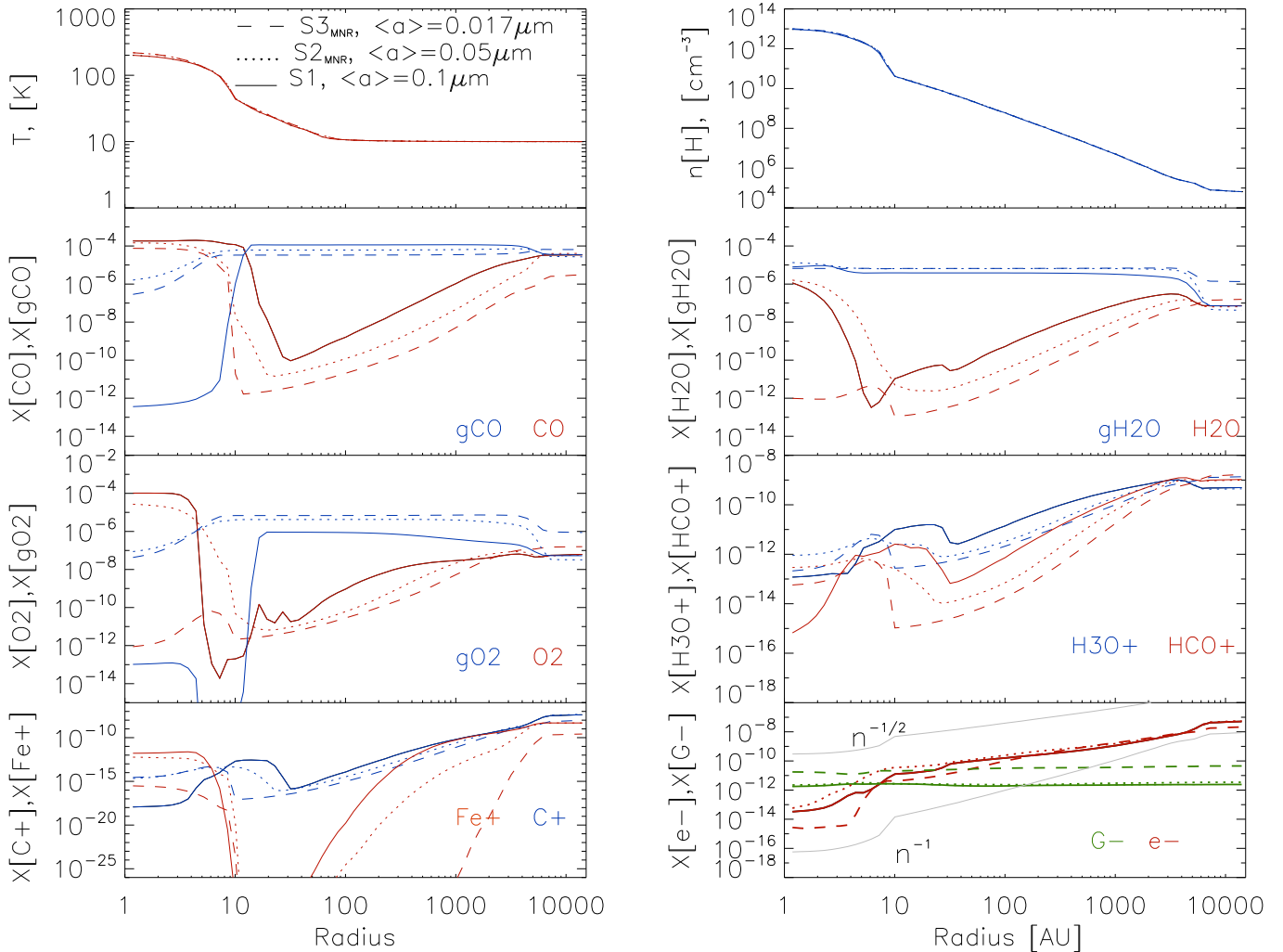


Fig. 6. Impact of dust size properties on selected chemical abundances. Same lay-out as in fig. 2. Solid line shows fiducial model (S1), dotted line shows the model S2_{MNR} and dashed line for S3_{MNR}, at t_0 . Abundances from model S5 and S4 are not overplotted for the sake of readability.

the adiabatic phase of collapse. Thus, the total abundance $X[\text{CO}]$ increases during the long (isothermal) phase of collapse due to gas-phase reactions, despite their inefficiency in a dark and poorly ionized cloud. In fig. 8, $X[\text{CO} + \text{gCO}]$ is uniform with radius down to the location where the gas is heated up to 25K - 60K. The amount of both gaseous and solid CO differs when the dust properties are changed. From this fact and from the comparison displayed in fig. 8 we conclude that the dust properties (number, size and distribution slope) have a strong impact on the CO abundance.

We conclude that it is worth to consider the effect of dust growth during the isothermal phase of the collapse ($T < 25\text{K}$, $t \leq 10^5$ yrs, e.g. Ormel et al. 2009, 2011). After the onset of the adiabatic phase, one can safely work with fixed dust population and concentrate more on dynamical chemistry. Our experiments make clear the importance of the dust modelling for constructing the synthetic collapse CO maps. The question of dust growth on the timescale of 10^5 years or longer during the isothermal phase of collapse shall be addressed in future work.

3.5. Limitations of the chemical module

There are several limitations in our dynamical chemical solver that can potentially affect the estimate of ionisation and thus the resulting magnetic diffusivities. We discuss below the three main limitations and defer their implementation in our model to future work.

First, we assume that the grain size distribution can be represented by a single mean size. Kunz & Mouschovias (2009) show that the dust size distribution should be described by at least five bins to have a convergence of less than 1% in the abundances.

Second, we consider single-charged grains whereas they can hold multiple electric charges (Draine & Sutin 1987; Dzyurkevich et al. 2013). Although multiple charged grains are scarce in dense cores (Umebayashi & Nakano 1980), they play an important role in the ionisation budget. In the same line, Marchand et al. (2016) show that charge transfer between grains has a first order effect for densities larger than $10^{10} - 10^{11} \text{ cm}^{-3}$ and that it becomes even more important in the case of multiple charge. Currently, chemical models are limited by numerical difficulties because of the

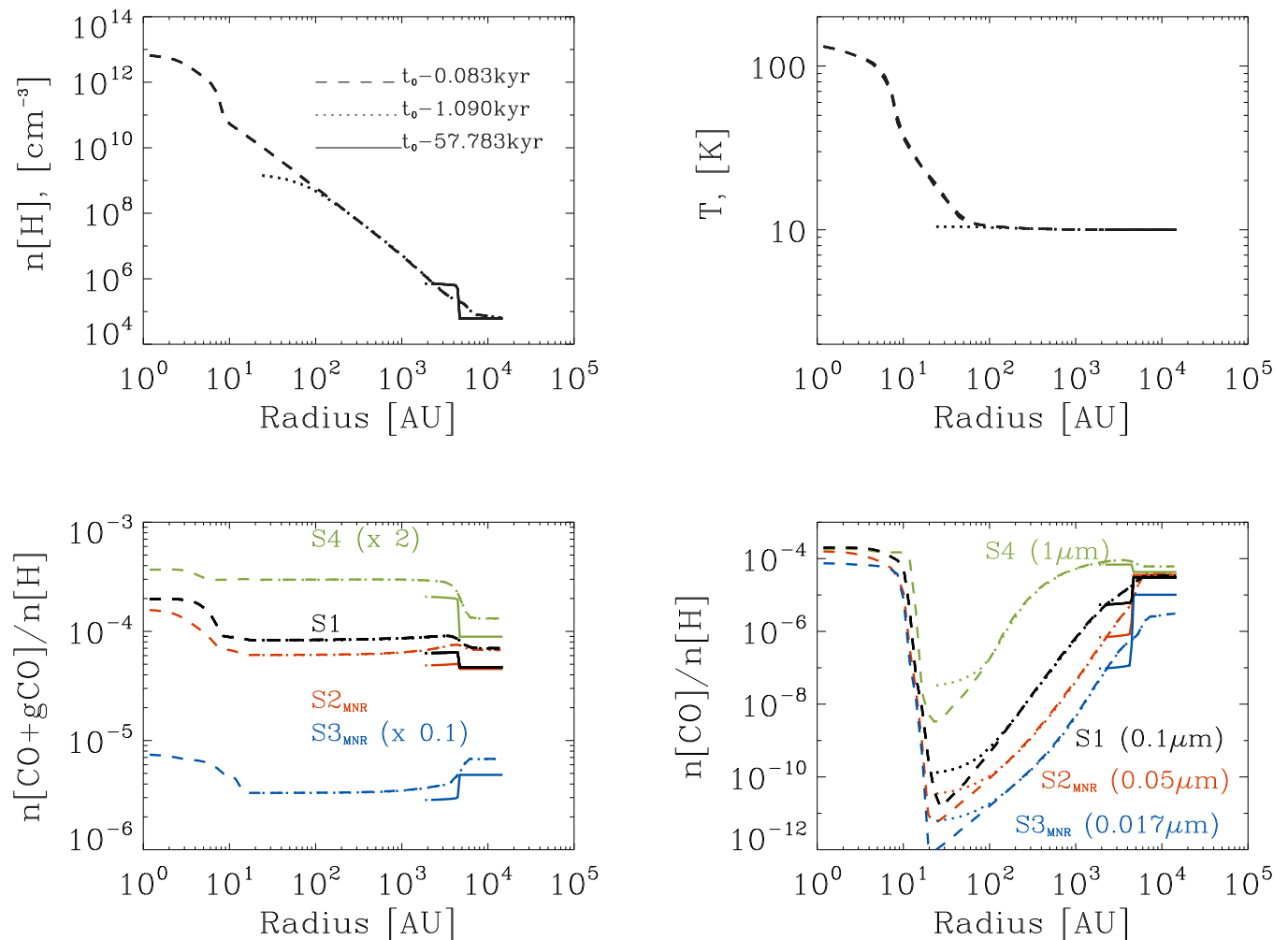


Fig. 8. Radial profiles of gas density, temperature and $X[\text{CO} + \text{gCO}]$ and $X[\text{CO}]$ abundances during the collapse starting from initial condition to t_0 (FHSC formation), for different dust sizes, i.e. models S1, S2_{MNR} and S3_{MNR}, and S4. Note, that the relative total CO abundance is multiplied by a factor 2 in case of S4 and by 0.1 in case of S3_{MNR}.

large dynamical range in the abundance of multiple charged grains, which is hard to handle in classical matrix inversion methods such as DVODE. Analytical models have been developed to treat multiple charges but they lack charge transfer between grains (e.g. Draine & Sutin 1987), or force the assumption of the constant ion mass (Okuzumi 2009).

Last, we do not account for the variations of the CR ionisation rate deep inside the collapsing core. Padovani et al. (2013, 2014) studied the propagation of CR along magnetic fields lines in collapsing cores, accounting for the effect of CR energy loss and magnetic mirroring.

4. Conclusion

We present the first time 3D chemo-dynamical radiation-hydrodynamics simulations of $1 M_{\odot}$ isolated dense core collapse. Such calculations are expensive but feasible, as demonstrated in this paper. The physical setup includes radiative hydrodynamics and dynamical evolution of a chemical network. In order to perform those simulations, we merged the multi-dimensional adaptive-mesh-

refinement code RAMSES and the thermo-chemistry Paris-Durham shock (PDS) code. We simulate the formation of the first hydro-static core and the co-evolution of 56 species, mainly describing H-C-O chemistry for the sake of computational feasibility.

The two key aspects of using the chemistry module within the RHD collapse simulation are: First, the observation-oriented aspect of how well the CO abundance can be computed in chemo-dynamical collapse simulations; Second is the theory-oriented aspect of how accurate our computation of magnetic diffusivities can be done in such chemo-dynamical collapse simulations. We use a spherical collapse setup and perform a parameter study, to study the dependence of CO abundances on the free-fall time and on the dust size, as well as the effect of dust properties on the ionisation deep inside the core.

In this paper we summarize the findings of the observation-oriented aspect:

- We have systematically tested the reduced chemical network against a well-established full gas-grain network.

We show that by using a compact set of reactions, one can get a pretty good match with a much more complex network. This saves computational time and enables the chemo-dynamical RHD simulations of the cloud collapse in 3D.

- We follow in detail the time-dependent formation of the first hydro-static core, until the central temperature of about 800 K and density of about 10^{13} cm^{-3} were reached. After that, we use the output physical structure and apply the static gas-grain chemistry with an extended set of reactions. We find that gas-grain chemistry post-processing can lead to one order of magnitude lower CO gas-phase abundances compared to the dynamical chemistry, with strongest effect during the isothermal phase of collapse.
- The duration of the collapse (i.e. free-fall time) has little effect on the chemical abundances for our choice of parameters. For mean grain sizes of $1 \mu\text{m}$ and larger, the gas-dust interaction timescales become longer than the representative dynamical timescales, which affects the pace of molecular depletion and makes dynamical chemistry a must.
- Dust grain mean radius and dust size distribution are crucial parameters to estimate chemical abundances. Varying the dust size from 0.02 to $0.1 \mu\text{m}$ changes the gaseous CO and water abundances by up to 2 orders in magnitude.

In accompanying paper, we concentrate on the effect of the dust properties on the magnetic diffusivities in the cloud. Dust mean size and size distribution have a strong effect on chemical abundances and hence on the ionization degree and magnetic dissipation.

Dynamical chemical evolution is required to describe the CO gas phase abundance (as well as the CO ice formation). Linking the chemical evolution to the careful treatment of the dust properties is of primary importance, regarding the recent observational and theoretical evidences of dust grain growth in the envelope of protostellar cores. Summarizing our finding above, we conclude that proper accounting for dust grain growth into the collapse simulations can be as important as coupling the collapse with chemistry.

This proof-of-concept study opens new perspectives for future protostellar collapse numerical models, in which more complex initial conditions (e.g. rotation and/or turbulence) and self-consistent non-ideal MHD calculations will be investigated. Further chemical process, such as ice formation on the grain surface, should also be considered in the future.

References

- Aikawa, Y., Wakelam, V., Garrod, R. T., & Herbst, E. 2008, *ApJ*, 674, 984
- Anders, E. & Grevesse, N. 1989, *Geochim. Cosmochim. Acta*, 53, 197
- Andersen, M., Steinacker, J., Thi, W.-F., et al. 2013, *A&A*, 559, A60
- Belloche, A., Garrod, R. T., Müller, H. S. P., & Menten, K. M. 2014, *Science*, 345, 1584
- Bergin, E. A. & Tafalla, M. 2007, *ARA&A*, 45, 339
- Commerçon, B., Audit, E., Chabrier, G., & Chièze, J.-P. 2011a, *A&A*, 530, A13
- Commerçon, B., Debout, V., & Teyssier, R. 2014, *A&A*, 563, A11
- Commerçon, B., Hennebelle, P., Audit, E., Chabrier, G., & Teyssier, R. 2010, *A&A*, 510, L3
- Commerçon, B., Teyssier, R., Audit, E., Hennebelle, P., & Chabrier, G. 2011b, *A&A*, 529, A35
- Cravens, T. E. & Dalgarno, A. 1978, *ApJ*, 219, 750
- di Francesco, J., Evans, II, N. J., Caselli, P., et al. 2007, *Protostars and Planets V*, 17
- Draine, B. T. 1978, *ApJS*, 36, 595
- Draine, B. T. & Sutin, B. 1987, *ApJ*, 320, 803
- Dzyurkevich, N., Turner, N. J., Henning, T., & Kley, W. 2013, *ApJ*, 765, 114
- Elmegreen, B. G. 1979, *ApJ*, 232, 729
- Fiedler, R. A. & Mouschovias, T. C. 1993, *ApJ*, 415, 680
- Flower, D. R. & Pineau des Forêts, G. 2003, *MNRAS*, 343, 390
- Flower, D. R. & Pineau des Forêts, G. 2015, *A&A*, 578, A63
- Flower, D. R., Pineau Des Forêts, G., & Walmsley, C. M. 2007, *A&A*, 474, 923
- Fromang, S., Hennebelle, P., & Teyssier, R. 2006, *A&A*, 457, 371
- Furuya, K., Aikawa, Y., Tomida, K., et al. 2012, *ApJ*, 758, 86
- Glover, S. C. O., Federrath, C., Mac Low, M.-M., & Klessen, R. S. 2010, *MNRAS*, 404, 2
- Godard, B., Falgarone, E., & Pineau Des Forêts, G. 2009, *A&A*, 495, 847
- Grassi, T., Bovino, S., Gianturco, F. A., Baiocchi, P., & Merlin, E. 2012, *MNRAS*, 425, 1332
- Grassi, T., Bovino, S., Schleicher, D., & Gianturco, F. A. 2013, *MNRAS*, 431, 1659
- Gredel, R., Lepp, S., & Dalgarno, A. 1987, *ApJ*, 323, L137
- Herbst, E. & Osamura, Y. 2008, *ApJ*, 679, 1670
- Hincelin, U., Wakelam, V., Commerçon, B., Hersant, F., & Guilloteau, S. 2013, *ApJ*, 775, 44
- Kunz, M. W. & Mouschovias, T. C. 2009, *ApJ*, 693, 1895
- Larson, R. B. 1969, *MNRAS*, 145, 271
- Lefèvre, C., Pagani, L., Juvela, M., et al. 2014, *A&A*, 572, A20
- Lesaffre, P., Belloche, A., Chièze, J.-P., & André, P. 2005, *A&A*, 443, 961
- Lesaffre, P., Chièze, J.-P., Cabrit, S., & Pineau des Forêts, G. 2004, *A&A*, 427, 147
- Lesaffre, P., Pineau des Forêts, G., Godard, B., et al. 2013, *A&A*, 550, A106
- Machida, M. N., Inutsuka, S.-i., & Matsumoto, T. 2007, *ApJ*, 670, 1198
- Marchand, P., Masson, J., Chabrier, G., et al. 2016, *A&A*
- Maret, S., Bergin, E. A., & Tafalla, M. 2013, *A&A*, 559, A53
- Masson, J., Teyssier, R., Mulet-Marquis, C., Hennebelle, P., & Chabrier, G. 2012, *ApJS*, 201, 24
- Mathis, J. S., Rumpl, W., & Nordsieck, K. H. 1977, *ApJ*, 217, 425
- Minerbo, G. N. 1978, *J. Quant. Spec. Radiat. Transf.*, 20, 541
- Okuzumi, S. 2009, *ApJ*, 698, 1122
- Ormel, C. W., Min, M., Tielens, A. G. G. M., Dominik, C., & Paszun, D. 2011, *A&A*, 532, A43
- Ormel, C. W., Paszun, D., Dominik, C., & Tielens, A. G. G. M. 2009, *A&A*, 502, 845
- Ossenkopf, V. 1993, *A&A*, 280, 617
- Padovani, M. & Galli, D. 2011, *A&A*, 530, A109
- Padovani, M., Galli, D., Hennebelle, P., Commerçon, B., & Joos, M. 2014, *A&A*, 571, A33
- Padovani, M., Hennebelle, P., & Galli, D. 2013, *A&A*, 560, A114
- Pagani, L., Steinacker, J., Bacmann, A., Stutz, A., & Henning, T. 2010, *Science*, 329, 1622
- Semenov, D., Henning, T., Helling, C., Ilgner, M., & Sedlmayr, E. 2003, *A&A*, 410, 611
- Semenov, D., Hersant, F., Wakelam, V., et al. 2010, *A&A*, 522, A42
- Steinacker, J., Ormel, C. W., Andersen, M., & Bacmann, A. 2014, *A&A*, 564, A96
- Steinacker, J., Pagani, L., Bacmann, A., & Guieu, S. 2010, *A&A*, 511, A9
- Teyssier, R. 2002, *A&A*, 385, 337
- Teyssier, R., Fromang, S., & Dormy, E. 2006, *Journal of Computational Physics*, 218, 44
- Umebayashi, T. & Nakano, T. 1980, *PASJ*, 32, 405
- Valdivia, V. & Hennebelle, P. 2014, *A&A*, 571, A46
- Vaytet, N., Audit, E., Chabrier, G., Commerçon, B., & Masson, J. 2012, *A&A*, 543, A60
- Visser, R., Doty, S. D., & van Dishoeck, E. F. 2011, *A&A*, 534, A132
- Visser, R., van Dishoeck, E. F., Doty, S. D., & Dullemond, C. P. 2009, *A&A*, 495, 881
- Wakelam, V., Herbst, E., Loison, J.-C., et al. 2012, *ApJS*, 199, 21
- Wiebe, D., Semenov, D., & Henning, T. 2003, *A&A*, 399, 197
- Wolfire, M. G., Hollenbach, D., McKee, C. F., Tielens, A. G. G. M., & Bakes, E. L. O. 1995, *ApJ*, 443, 152

Appendix A: Approximate treatment of the dust-size distribution

In our chemical module, we want to take into account the effect of dust-size distribution on the chemistry and to avoid high memory costs due to treatment of numerous size bins. Here, we trace the number densities only of species G0, G⁻ and G⁺. For simplicity, we neglect the multiple dust charges. In case of fixed dust size, the density of dust grain is simply defined as

$$n_{\text{dust}} = \frac{M_{\text{gas}} f_{\text{dg}}}{4/3\pi a^3 \rho_{\text{solid}}}, \quad (\text{A.1})$$

where a is the grain radius and ρ_{solid} is the internal density of the solid materials. We adopt a MRN size distribution $dn/da \propto a^{-3.5}$ (Mathis et al. 1977). Next, we have to choose a range of sizes: the minimum grain radius is $a_{\text{min}} = 0.01 \mu\text{m}$ and maximum radius $a_{\text{max}} = 0.3 \mu\text{m}$. For the chemistry, the rates of ion-dust or electron dust reactions are directly affected by number density of the dust. The total available surface of dust grains affects the rates of the freeze-out of species on dust. We can determine n_{dust} using Eq. A.1 after calculating the effective cubic radius $R3 = \langle a^3 \rangle$ from

$$R3 = \frac{\int_{a_{\text{min}}}^{a_{\text{max}}} a^3 a^{-3.5} da}{\int_{a_{\text{min}}}^{a_{\text{max}}} a^{-3.5} da} = 5 \frac{a_{\text{max}}^{0.5} - a_{\text{min}}^{0.5}}{a_{\text{min}}^{-2.5} - a_{\text{max}}^{-2.5}} \quad (\text{A.2})$$

Similarly, we can use the number-weighted squared radius $R2 = \langle a^2 \rangle$ for reactions sensitive to dust surface, like those in eq. 3 and eq. 4.

$$R2 = 2.5 \frac{a_{\text{min}}^{-0.5} - a_{\text{max}}^{-0.5}}{a_{\text{min}}^{-2.5} - a_{\text{max}}^{-2.5}}. \quad (\text{A.3})$$

The average grain radius is

$$\langle a \rangle = 2.5 \frac{a_{\text{min}}^{-1.5} - a_{\text{max}}^{-1.5}}{a_{\text{min}}^{-2.5} - a_{\text{max}}^{-2.5}} / 1.5. \quad (\text{A.4})$$

Number-weight grain radius and a scale factor between the $\langle a \rangle$ and $\langle \sqrt{R2} \rangle$ are needed for correction of the grain cross-section for mantles. Correction factor is $a_{\text{corr}} = \langle a \rangle / \sqrt{\langle R2 \rangle}$.

The next input parameter is the average distance between sites on the surface of the grain, $\Delta d_{\text{sites}} = 3.4d - 8 \text{ cm}$. Same number is adopted for the thickness of the layers of sites in the grain's mantle. Number of sites on a single grain of average size is calculated as

$$S = \frac{4\pi \langle a \rangle^2}{(\Delta d_{\text{sites}})^2}, \quad (\text{A.5})$$

whereas $N_{\text{sites}} = (\Delta d_{\text{sites}})^{-2}$ is a site density in cm^{-2} , taken into account by calculation of the vibrational frequency in eq. 4.

Appendix B: Benchmark tests for reduced chemical network

In this appendix, we compare the results of the full chemical network and of our reduced network in RAMSES. First we consider the case of pure gas-chemistry (fig. B.1). We then add step-by-step adsorption on the grain surface (fig. B.2, CR-desorption (fig. B.3). The agreement between both networks is excellent.

Appendix C: Advection test

We made minor changes in the RAMSES code in the advection scheme. Gas density is advected following the continuity equation

$$\frac{\partial \rho}{\partial t} + \nabla(\mathbf{u}\rho) = 0. \quad (\text{C.1})$$

It is possible to define a number of passive scalars in RAMSES, which are always considered as relative specie abundances, $n_{\text{specie}}/n_{\text{gas}}$, and are advected in a different way to the gas density,

$$\frac{\partial \rho}{\partial t} + \mathbf{u}\nabla(\rho) = 0. \quad (\text{C.2})$$

As we want to advect the absolute number density of chemical species, we modified the solver to treat the N_{species} of chemical species in the same way as the gas density, i.e. not as passive scalars. To test the modifications, we create a simple test. All N_{species} variables for chemistry are replaced with some arbitrary densities $n = 10^{-i+1}n_{\text{gas}}$, where $i = 0, N_{\text{species}} - 1$ is a number of variable. In our test simulation, those densities are advected during the whole length of simulations such as S1 (3). We have observed that those 'chemical species' are perfectly advected and keep the initial constant fraction of gas number density during whole collapse simulation to FHSC (first hydro-static core).

Appendix D: Initial conditions: Abundances of CO for the broad range of gas parameters

Here we present the abundances of CO and its ice, generated by ALCHEMIC code for a following set of parameters. For the fixed visual extinction $A_V = 20$, the temperature ranges from 10K to 1000K, gas number density is varied from 2×10^2 to $2 \times 10^{12} \text{cm}^{-3}$. The chemical abundances were evolved up to $5 \times 10^5 \text{yrs}$ for those ranges in density and temperature, which results in the 3D data table. We are interested in how sensitive is the CO abundance to the density of the gas in our initial condition for the collapse. Thus, we plot temporal evolution of relative abundance of CO ($n[\text{CO}]/n[\text{H}]$, $n[\text{gCO}]/n[\text{H}]$), for various gas densities and for fixed temperature of 10K. We observe that the total amount of CO is independent from the density of the prestellar core, as long as its temperature is not larger than 10K (fig. D.1). The gaseous CO is less abundant for larger gas densities, and it is faster depleted onto the dust surface for the denser gas (fig. D.1 left, black lines).

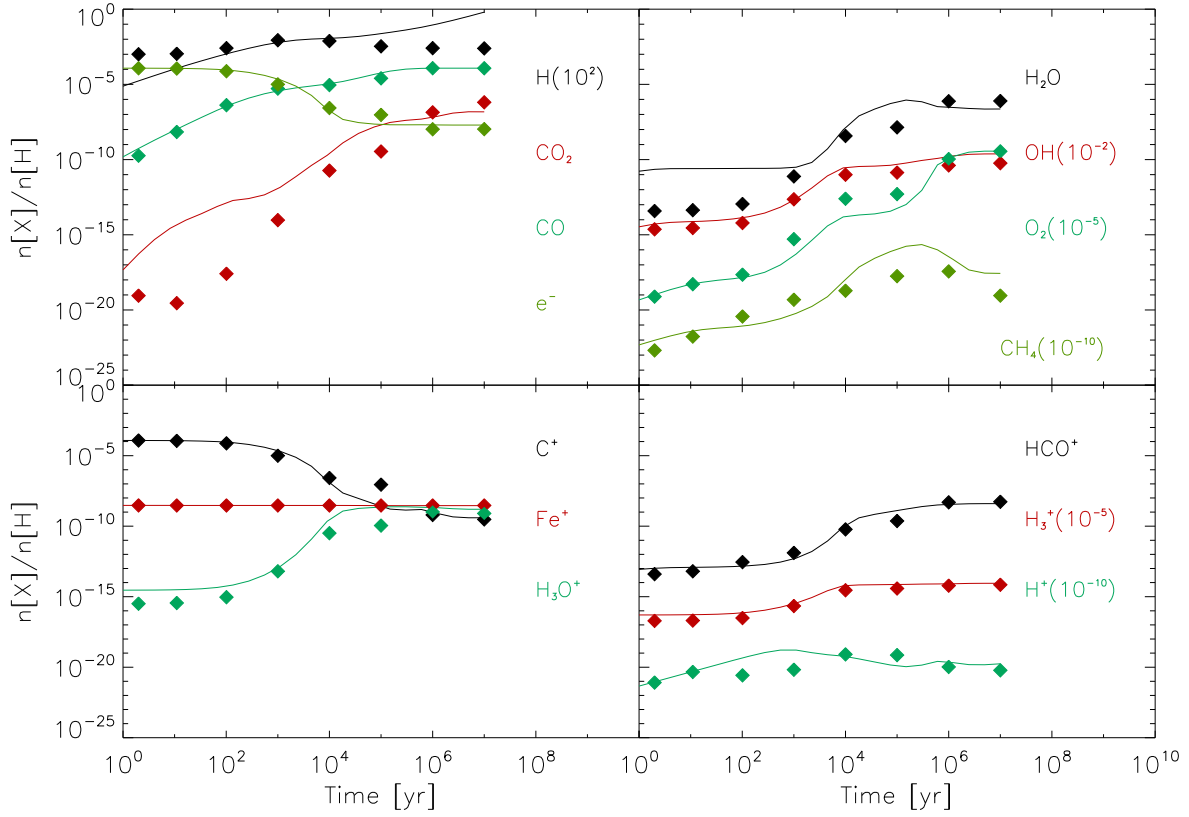


Fig. B.1. Time evolution of selected chemical species without dust grain reactions: Solid line shows the case of full chemical network in ALCHEMIC, diamonds the case of reduced network in RAMSES.

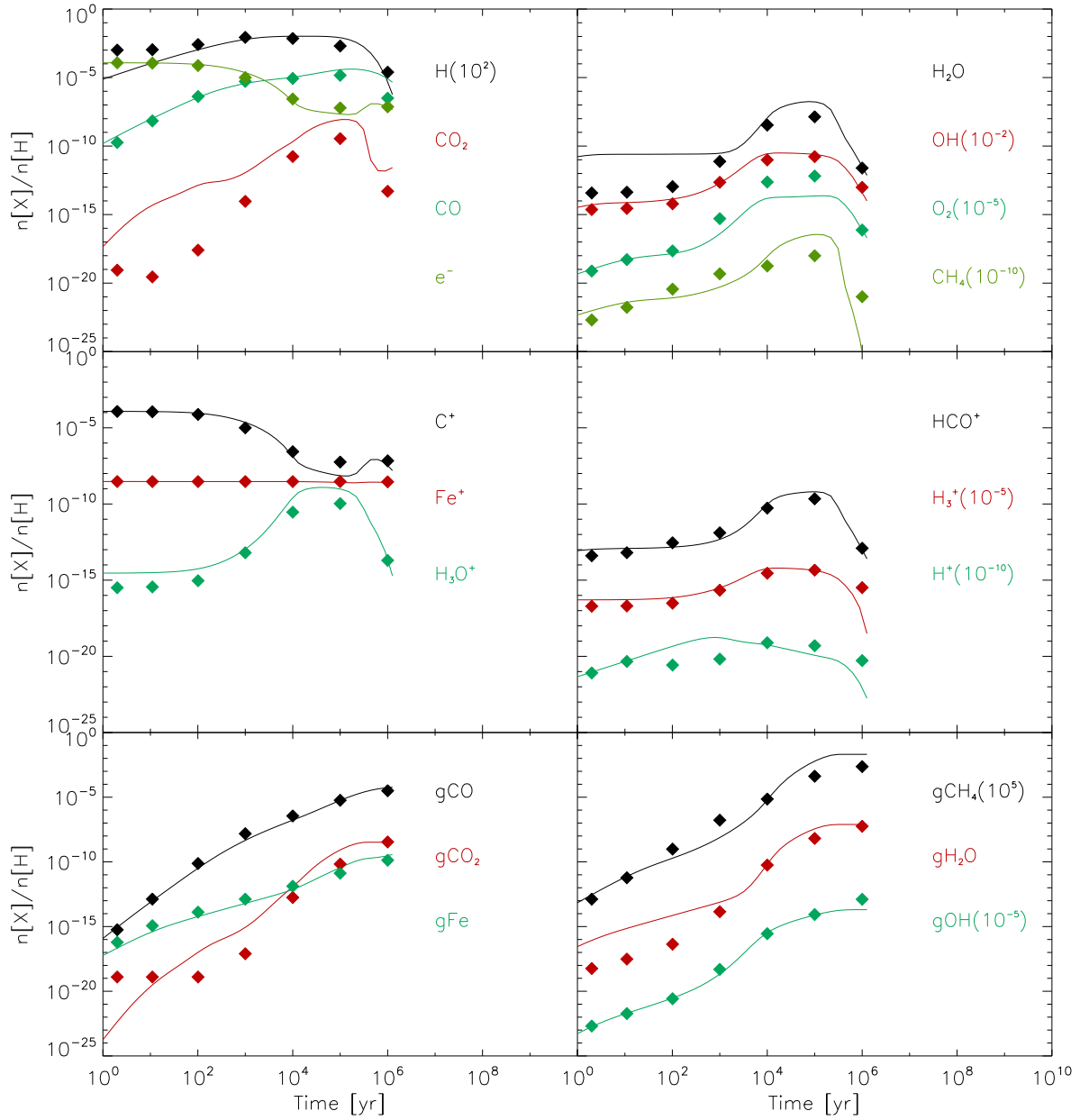


Fig. B.2. Time evolution of selected species for gas-phase reactions with freeze-out reactions: Solid line shows full chemical network in ALCHEMIC, diamonds the reduced network in RAMSES.

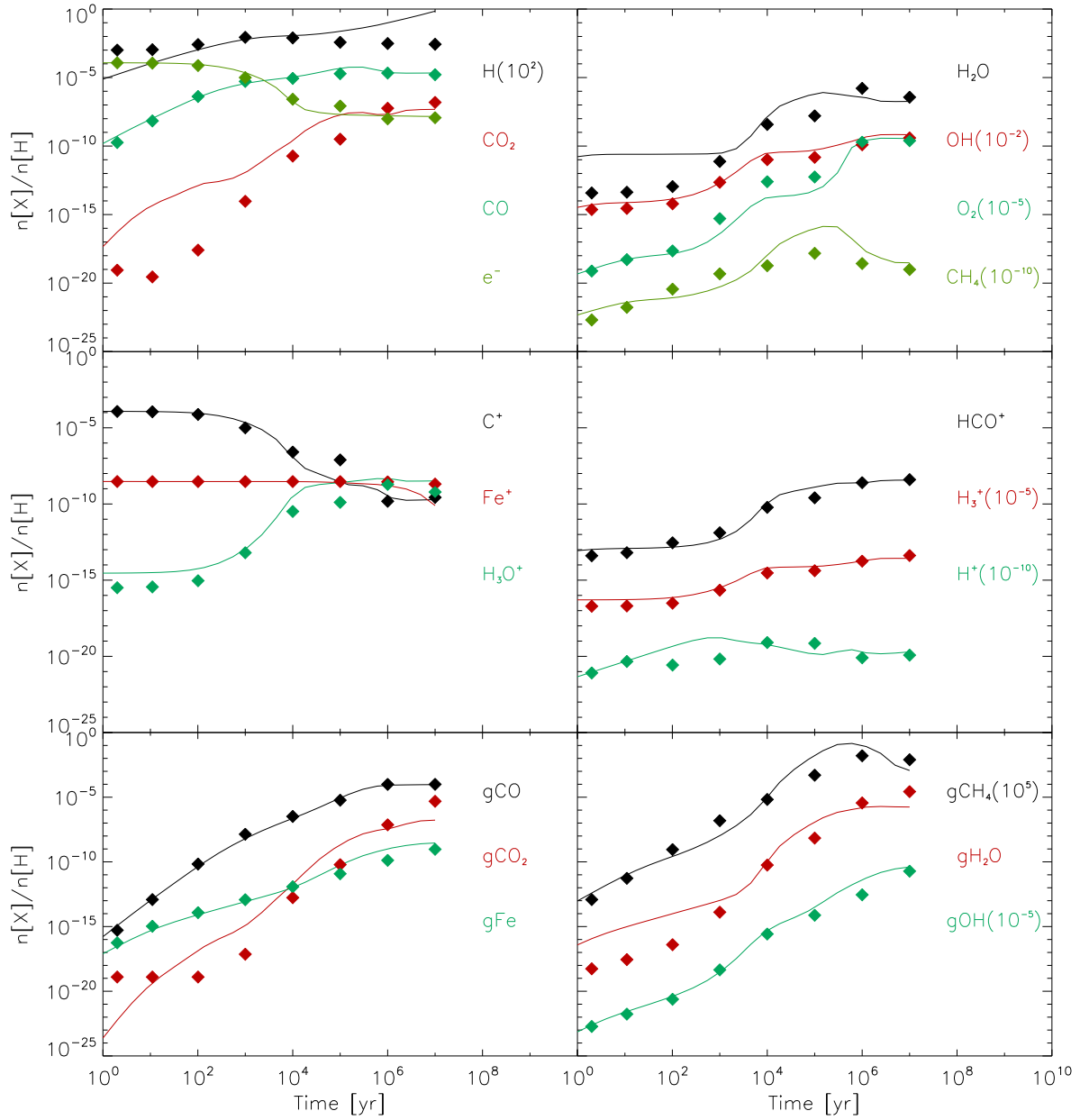


Fig. B.3. Time evolution of selected species for gas-phase chemistry with freeze-out and CR desorption reactions: Solid line shows full chemical network in ALCHEMIC, diamonds the reduced network in RAMSES.

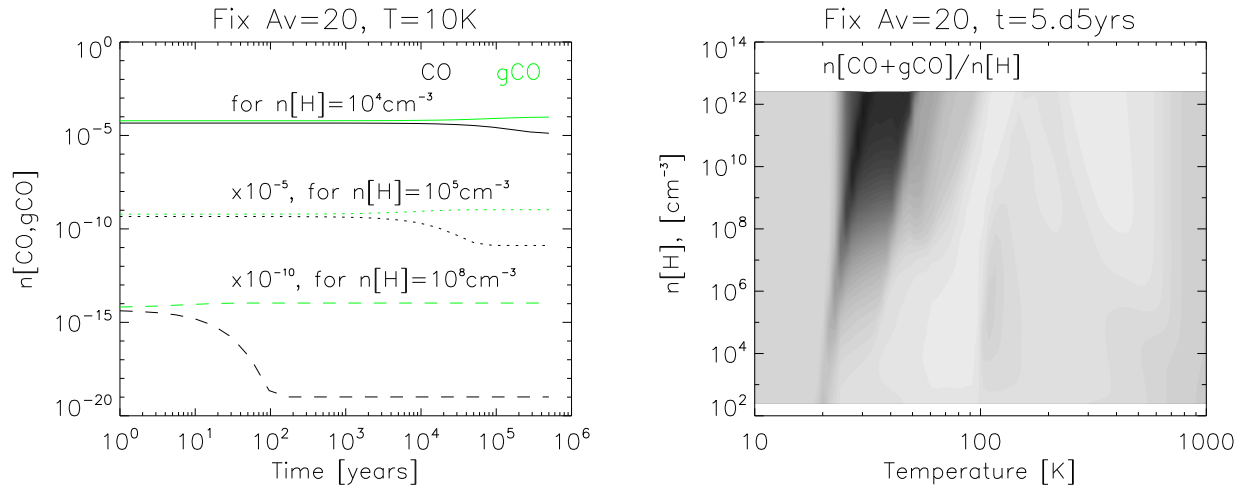


Fig. D.1. Left: Time evolution of CO in gas and solid phases, performed for three different gas densities which are shown in solid, dotted and dashed lines. Right: total CO abundance shown in $(n[\text{H}], T)$ space. Visual extinction is fixed to $A_v = 20$ for both panels. These data are generated with full chemical network **ALCHEMIC** (credits to D. Semenov).